Impeding Macrophage Entry into Hypoxic Tumor Areas by Sema3A/Nrp1 Signaling Blockade Inhibits Angiogenesis and Restores Antitumor Immunity

Impeding Macrophage Entry into Hypoxic Tumor Areas by Sema3A/Nrp1 Signaling Blockade Inhibits Angiogenesis and Restores Antitumor Immunity

Andrea Casazza[1, 2], Damya Laoui[3, 4], Mathias Wenes[1, 2], Sabrina Rizzolio[5], Nicklas Bassani[1, 2], Marco Mambretti[1, 2], Sofie Deschoemaeker[1, 2], Jo A. Van Ginderachter[3, 4], Luca Tamagnone[5], Massimiliano Mazzone[1, 2, ,]

[1] Laboratory of Molecular Oncology and Angiogenesis, Vesalius Research Center, VIB, 3000 Leuven, Belgium
[2] Laboratory of Molecular Oncology and Angiogenesis, Department of Oncology, Vesalius Research Center, KU Leuven, 3000 Leuven, Belgium
[3] Laboratory of Myeloid Cell Immunology, VIB, 1050 Brussels, Belgium
[4] Laboratory of Cellular and Molecular Immunology, Department of Molecular and Cellular Interactions, Vrije Universiteit Brussel, 1050 Brussels, Belgium
[5] Institute for Cancer Research at Candiolo, Department of Oncology, University of Torino, 10060 Candiolo, Torino, Italy

Summary

Recruitment of tumor-associated macrophages (TAMs) into avascular areas sustains tumor progression; however, the underlying guidance mechanisms are unknown. Here, we report that hypoxia-induced Semaphorin 3A (Sema3A) acts as an attractant for TAMs by triggering vascular endothelial growth factor receptor 1 phosphorylation through the associated holoreceptor, composed of Neuropilin-1 (Nrp1) and PlexinA1/PlexinA4. Importantly, whereas Nrp1 levels are downregulated in the hypoxic environment, Sema3A continues to regulate TAMs in an Nrp1-independent manner by eliciting PlexinA1/PlexinA4-mediated stop signals, which retain them inside the hypoxic niche. Consistently, gene deletion of Nrp1 in macrophages favors TAMs' entrapment in normoxic tumor regions, which abates their pro-angiogenic and immunosuppressive functions, hence inhibiting tumor growth and metastasis. This study shows that TAMs' heterogeneity depends on their localization, which is tightly controlled by Sema3A/Nrp1 signaling.

Graphical Abstract

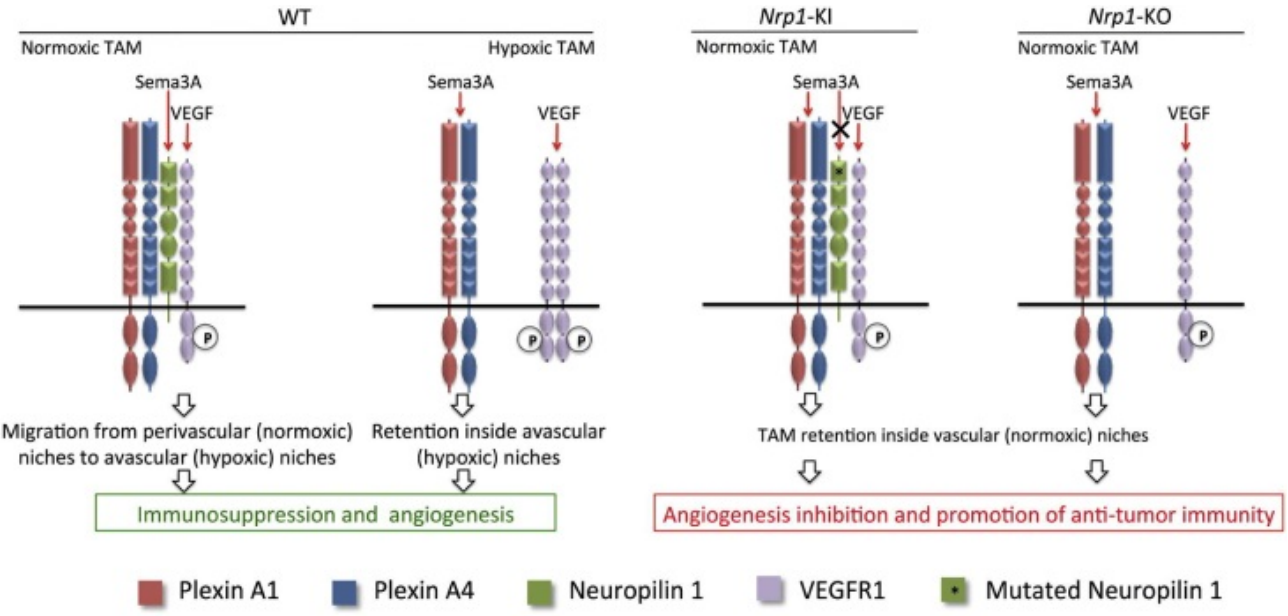

Significance

TAM infiltration of human cancers was reported to correlate with opposed prognoses because TAMs can be either pro- or antitumoral. Here, we show that TAMs' localization into hypoxic tumor areas is controlled by a Sema3A/Neuropilin-1 signaling axis, leading to PlexinA1/PlexinA4-dependent VEGFR1 activation. Once in the hypoxic environment, TAMs are arrested because of Nrp1-independent PlexinA1/PlexinA4-mediated stop signals. We found that confining TAMs inside normoxic regions by blunting the Sema3A/Neuropilin-1 pathway restores anti-tumor immunity and abates angiogenesis, overall inhibiting tumor growth and metastasis. These results underscore the predictive value of macrophage association with tumor hypoxia and suggest alternative approaches to hijack TAMs against cancer by modulating their localization within the tumor, and thus their phenotype.

Introduction

Inflammatory / immune responses mostly involve the recruitment of circulating monocytes to specific locations, such as intratumoral areas, bacterial entry sites, arthritic joints, infarcted lesions, or atherosclerotic plaques (Eltzschig and Carmeliet, 2011). In particular, macrophages infiltrating the tumor, named tumor-associated macrophages (TAMs), represent the most abundant stromal component of many cancer types and the presence of extensive TAM infiltration, often but not always, correlates with poor prognosis in a variety of human carcinomas (De Palma and Lewis, 2013 and Johansson et al., 2008). This is because TAMs entail protumoral functions, but they were also reported to be antitumoral (Biswas and Mantovani, 2010, Coussens et al., 2013 and Johansson et al., 2008). Such opposed TAM phenotypes occupy distinct niches in the tumor, thus raising the question whether this may reflect "education" of the macrophages by specific signals in the tumor microenvironment and/or whether TAM subsets might derive from distinct macrophage precursors (Murdoch and Lewis, 2005).

Neuropilin-1 (Nrp1) was originally identified as a receptor for class-3 semaphorins controlling neuronal guidance and axonal growth (Gu et al., 2003 and Kolodkin et al., 1997). Besides playing a decisive role in the developing nervous system, Nrp1 is expressed in a variety of non-neural cells and can modulate multiple physiological and pathological processes (Gerhardt et al., 2004, Gu et al., 2003, Hayashi et al., 2012, Liang et al., 2007 and Soker et al., 1998). Preclinical data suggest that blockade of Nrp1 suppresses tumor growth by inhibiting angiogenesis or by impairing survival and proliferation in a variety of cancer cell types (Hong et al., 2007, Liang et al., 2007 and Pan et al., 2007).

Nrp1 is also widely expressed in lymphoid and myeloid cells (Bruder et al., 2004, Fantin et al., 2010 and Pucci et al., 2009). In vitro and in vivo studies have identified a regulatory role of this molecule in immune responses, cell proliferation, chemotaxis, and cytokine production of T cells and dendritic cells (DCs) (Catalano, 2010, Catalano et al., 2006, Delgoffe et al., 2013, Hansen et al., 2012, Takamatsu et al., 2010 and Tordjman et al., 2002). Other studies, also from our laboratory, have described *Nrp1* as a marker of pro-angiogenic and pro-arteriogenic macrophages in physiological and pathological conditions (Fantin et al., 2010, Pucci et al., 2009, Rolny et al., 2011 and Takeda et al., 2011). Nevertheless, the functional relevance of this molecule in macrophages is not known.

By using genetic tools and several tumor mouse models, we study how Nrp1 controls TAMs' entry into hypoxic regions in response to its ligand Semaphorin 3A.

Results

Loss of Nrp1 in Macrophages Inhibits Tumor Progression

By intercrossing *Nrp1* floxed mice with LysM-Cre mice, we generated LysM-Cre;*Nrp1L*^{l}*L* mice where *Nrp1*expression is reduced by 92% in TAMs and 81% in their monocyte precursors, but less than 60% in tumor-associated neutrophils (TANs) or DCs (Figure S1A available online). Compared to littermate controls (LysM-Cre;*Nrp1*+/+; wild type [WT] in short), LysM-Cre;*Nrp1L*^{l}*L* mice were normal and had similar blood counts (Table S1 and Fantin et al., 2013); however, the implantation of subcutaneous Lewis lung carcinomas (LLC) resulted in 60% smaller tumors and 55% fewer pulmonary metastases (Figures 1A–1C). Tumor apoptosis was increased in LysM-Cre;*Nrp1L*^{l}*L* mice (Figure S1B) but proliferation was unchanged (Figure S1C). Tumor vessel area, density and branching points, together with vessel perfusion, were strongly decreased in LysM-Cre;*Nrp1L*^{l}*L* mice (Figures 1D–1I).

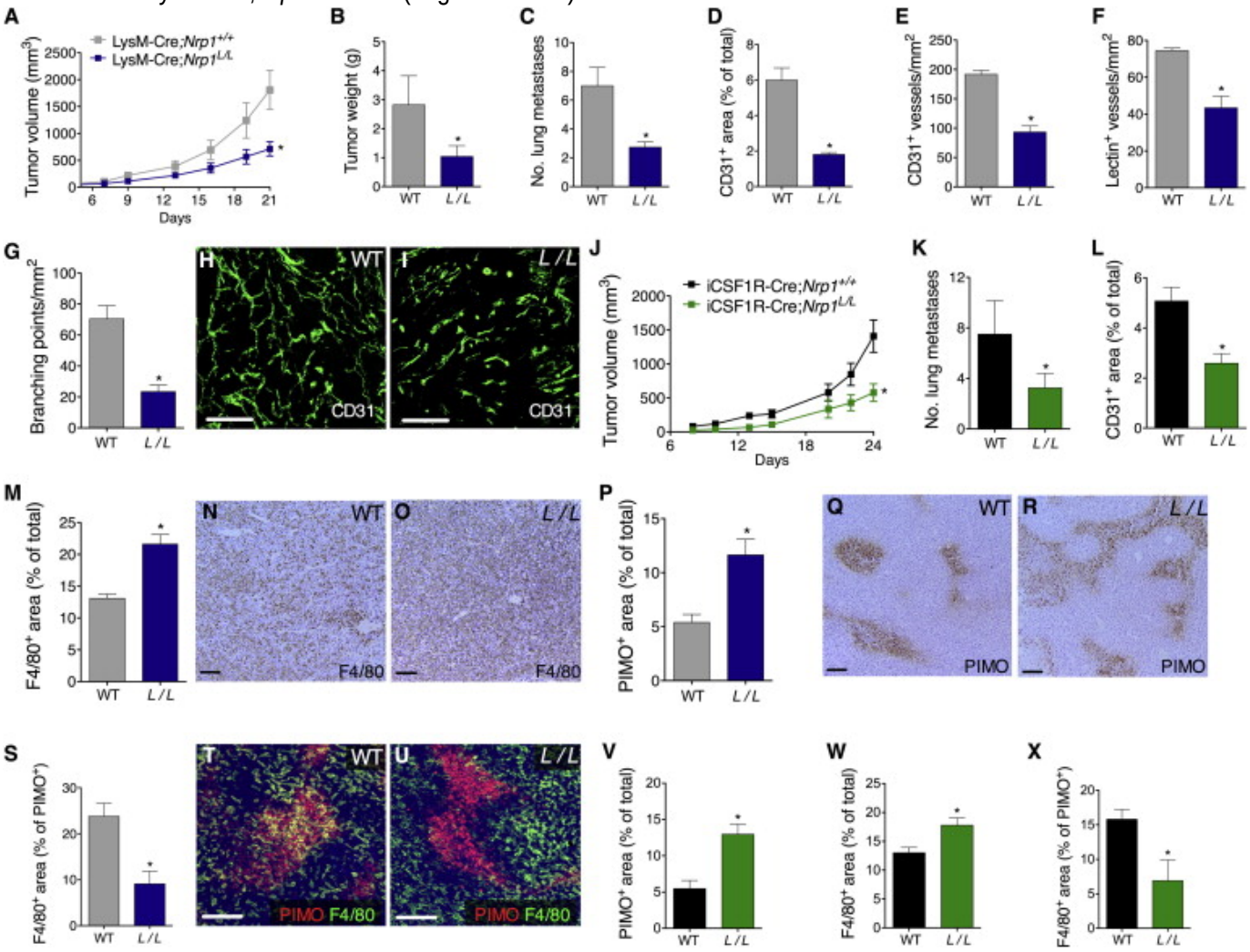

Figure 1.

Loss of *Nrp1* in TAMs Inhibits Their Entry into Hypoxic Niches

(A–C) Subcutaneous LLC tumor growth (A), weight (B), and lung metastases (C) in mice with myeloid cell-specific deletion of *Nrp1* (LysM-Cre;*Nrp1L*^{l}*L*; *L/L* in short) and controls (LysM-Cre;*Nrp1*+/+; WT in short).

(D–F) Tumor vessel area (D), density (E), and perfusion (F) in WT and LysM-Cre;*Nrp1L*^{l}*L* (*L/L*) mice.

(G–I) Vessel branching quantification (G) and micrographs (H and I) on CD31-stained LLC tumor thick-sections.

(J–L) Subcutaneous LLC tumor growth (J), lung metastases (K), and tumor vessel density (L) in mice with macrophage-specific deletion of *Nrp1* (iCSF1R-Cre;*Nrp1L*^{l}*L*; *L/L* in short) and controls (iCSF1R-Cre;*Nrp1*+/+; WT in short).

(M–O) F4/80 quantification (M) and micrographs (N and O) showing TAM infiltration of end-stage subcutaneous LLC tumors in WT and LysM-Cre;*Nrp1L*^{l}*L* (*L/L*) mice.

(P–R) Quantification (P) and micrographs of pimonidazole (PIMO)-stained LLC tumor sections in WT and LysM-Cre;*Nrp1L*^{l}*L* (*L/L*) mice (Q and R).

(S–U) Morphometric quantification (S) and micrographs (T,U) of LLC tumor sections stained for F4/80 and PIMO, showing TAM infiltration of hypoxic tumor regions in WT and LysM-Cre;*Nrp1L*^{l}*L* (*L/L*) mice.

(V–X) Tumor hypoxia (V) and TAM infiltration of the overall tumor sections (W) or of hypoxic tumor regions (X) in WT and iCSF1R-Cre;*Nrp1L*^{l}*L* (*L*/*L*) mice.

All experiments, n = 8. $^{*}p < 0.05$ versus WT. Scale bars: 100 μm. All graphs show mean ± SEM. See also Figure S1 andTable S1.

To achieve specific deletion of *Nrp1* in macrophages, but not in other myeloid cells (Figure S1D and Qian et al., 2011), we intercrossed *Nrp1* floxed mice with the tamoxifen-inducible iCSF1R-Cre line, thus generating iCSF1R-Cre;*Nrp1L*^{l}*L* mice. Acute deletion of *Nrp1* shortly before LLC tumor injection, abated tumor growth, metastasis, and vessel formation to a similar extent as in LysM-Cre;*Nrp1L*^{l}*L* mice (Figures 1J–1L; Figures S1E and S1F). Thus, *Nrp1* loss in TAMs inhibits cancer progression and angiogenesis.

Loss of Nrp1 in TAMs Prevents Their Entry into Hypoxic Niches

To quantify tumor infiltration of myeloid cells in WT and LysM-Cre;*Nrp1L/L* mice, we stained tumor sections for the pan-myeloid marker CD11b. Tumors in LysM-Cre;*Nrp1L*^{l}*L* mice were infiltrated with almost twice more myeloid cells than in the controls (Figures S1G–S1I). Among all the CD11b^{+} myeloid cells, only TAMs, but not TANs or DCs, were more abundant in LysM-Cre;*Nrp1L*^{l}*L* versus WT mice (Figures 1M–1O; Figure S1J). Increased TAM density was not associated to a difference in the frequency of total circulating monocytes or monocyte subsets ("inflammatory" CD115^{+}Ly6C^{high} versus "resident" CD115^{+}Ly6C^{low} monocytes), TAM proliferation, or TAM apoptosis (Figures S1J–S1M). Moreover, in a model of acute skin inflammation, macrophage infiltration was equally induced in both genotypes, suggesting that *Nrp1* deletion did not affect monocyte recruitment or their differentiation into macrophages (Figure S1N).

We reasoned that the rise of TAMs in LysM-Cre;*Nrp1L*^{l}*L* mice was due to increased tumor hypoxia (Eltzschig and Carmeliet, 2011 and Murdoch and Lewis, 2005), possibly resulting from reduced tumor perfusion. Indeed, the hypoxic tumor area was 2.2-times higher in LysM-Cre;*Nrp1L*^{l}*L* than in WT mice (Figures 1P and 1R). Conversely, at early stages (when tumor volume and weight were comparable in both genotypes), the amount of hypoxic areas as well as TAMs did not change (Figures S1O–S1R), suggesting that increased TAM infiltration in LysM-Cre;*Nrp1L*^{l}*L* mice was secondary to tumor progression and augmented hypoxia. Consistently, hypoxia-induced monocyte attractants such as *Ccl2*, *Csf1*, and *Csf2* were comparable in both genotypes at short term, but they were higher in LysM-Cre;*Nrp1L*^{l}*L* mice at the end stage, the time point when TAMs' frequency increases in these mice (Figures S1S–S1U). Strikingly, in LysM-Cre;*Nrp1L*^{l}*L* mice, TAMs were found mostly in normoxic (PIMO-negative) regions, and their accumulation inside hypoxic areas was instead greatly prevented both at early (Figure S1V) and end stage (Figures 1S–1U). In LysM-Cre;*Nrp1L*^{l}*L* mice as well, total hypoxic area and total density of TAMs in end-stage tumors were augmented but TAM accumulation within the hypoxic regions was reduced (Figures 1V–1X). Apoptosis and proliferation of WT and *Nrp1*-knockout (KO) TAMs or bone marrow-derived macrophages (BMDMs), cultured in either normoxia (21% O_2) or hypoxia (1% O_2) for 36 hr, did not differ (not shown). Altogether, these data indicate that Nrp1 is not directly involved in macrophage recruitment to the tumor but might rather be involved in TAM entry into hypoxic niches.

TAM Redistribution by Nrp1 Loss Hinders Orthotopic and Spontaneous Tumors.

Because the microenvironment strongly influences tumor responses (Blouw et al., 2003), we evaluated how*Nrp1* loss in TAMs affected the progression of several orthotopic tumors. First, we injected LLC cancer cells directly in the lungs. Sixteen days after injection, 47% of WT mice and only 8% of LysM-Cre;*Nrp1L*^{l}*L* mice died (Figure 2A). Of all the survivors, whole lung weight in WT mice was 63% higher than in LysM-Cre;*Nrp1L*^{l}*L* mice and tumor expansion in WT mice completely destroyed the structure of the pulmonary parenchyma whereas this was better preserved in LysM-Cre;*Nrp1L*^{l}*L* mice (Figures 2B–2D).

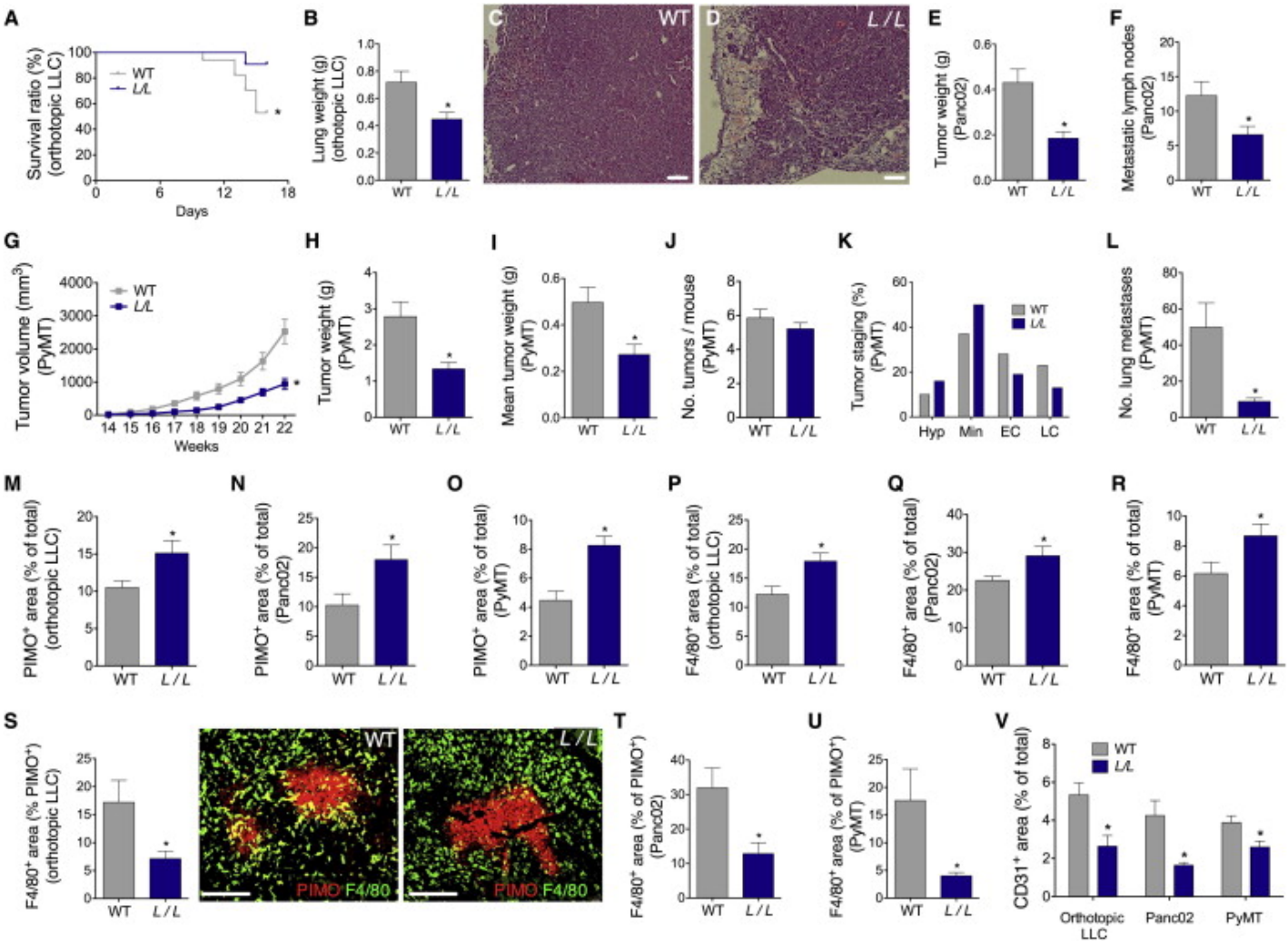

Figure 2.
Loss of *Nrp1* in TAMs Abates Orthotopic Tumor Growth and Metastasis
(A–D) Kaplan-Meier at 16 days (n = 11-17; A), lung weight (B), and pulmonary structure by hematoxylin and eosin staining (C and D) in WT and LysM-Cre;*Nrp1L*^{l}*L* (*L/L*) mice orthotopically implanted with LLC tumors (n = 7).
(E and F) Orthotopic Panc02 tumor weight (E) and number of metastatic mesenteric lymph nodes (F) in WT and LysM-Cre;*Nrp1L*^{l}*L* (*L/L*) mice. n = 9.
(G–J) Total tumor volume (G), total (H) and mean (I) tumor weight, and tumor incidence (J) in WT and LysM-Cre;*Nrp1L*^{l}*L*(*L/L*) mice intercrossed with a mouse strain developing spontaneous breast cancer (PyMT). n = 14.
(K) Frequency of hyperplastic (Hyp) or intraepithelial (Min) neoplastic mammary lesions compared to the frequency of early (EC) or late (LC) PyMT mammary carcinomas.
(L) Number of lung metastatic nodules arising from PyMT tumors.
(M–R) Hypoxic PIMO^{+} areas (M–O) and TAM accumulation (P–R) in the indicated tumor model.
(S–U) Quantification and representative images of TAMs in PIMO^{+} regions in the indicated tumor model.
(V) Tumor vessel area in the indicated tumor model.
$^{*}p < 0.05$ versus WT. Scale bars: 100 μm. All graphs show mean ± SEM.

Because pancreatic cancers expressing higher VEGF or Sema3A levels have worse prognosis (Biankin et al., 2012, Müller et al., 2007 and Niedergethmann et al., 2002), we injected Panc02 pancreatic cancer cells orthotopically in WT and LysM-Cre;*Nrp1L^{l}L* mice. Also in this case, end-stage tumor weight was reduced by 60% in LysM-Cre;*Nrp1L^{l}L* versus WT mice (Figure 2E). The number of metastatic lymph nodes in the mesentery of LysM-Cre;*Nrp1L^{l}L* mice was two times lower than that found in WT mice (Figure 2F).

To prevent inflammation caused by technical procedures (i.e., needle injection), we intercrossed WT and LysM-Cre;*Nrp1L^{l}L* mice with mice expressing the PyMT oncoprotein under the control of the mouse mammary tumor virus promoter (MMTV-PyMT), a mouse model that spontaneously develops multiple metastatic mammary gland carcinomas (Lin et al., 2003). In this genetic background, tumors reached end stage in 22-week-old control mice. LysM-Cre;*Nrp1L^{l}L* littermates had 50% smaller tumors (Figures 2G–2I). Although the overall tumor incidence did not differ between genotypes, LysM-Cre;*Nrp1L^{l}L* mice displayed more hyperplastic and intraepithelial neoplastic lesions but fewer early and late carcinomas (Figures 2J and 2K). Furthermore, lung metastases in these mice were 80% less than those in controls (Figure 2L).

Similar to what observed in subcutaneous LLC tumors, all these orthotopic models displayed higher tumor hypoxia and TAM infiltration in LysM-Cre;*Nrp1L^{l}L* than in WT mice (Figures 2M–2R); however, *Nrp1*-KO TAMs failed to enter hypoxic niches (Figures 2S–2U). This phenotype was associated with reduced tumor vascularization (Figure 2V). Altogether, these data show that TAM redistribution by loss of *Nrp1* is accompanied by a slower progression of several orthotopic tumors independently from their tissue of origin.

TAM Redistribution by Nrp1 Loss Restores Immunity and Reduces Angiogenesis

Because TAMs in LysM-Cre;*Nrp1L^{l}L* mice failed to enter hypoxic tumor regions, we studied the effect on their phenotype. Compared to WT TAMs, TAMs from LysM-Cre;*Nrp1L^{l}L* mice were less potent in promoting endothelial cell (EC) migration and in inducing the formation of EC capillary networks, either when co-cultured directly with ECs or upon stimulation of ECs with TAM-conditioned media (Figures 3A–3E; Figure S2A–S2D). Furthermore, TAMs from LysM-Cre;*Nrp1L^{l}L* mice released more nitric oxide (NO; Figure 3F), were more cytotoxic against cancer cells (Figure 3G), and displayed reduced T cell suppression (thus increasing T cell proliferation; Figure 3H). Notably, all these functions did not differ between WT and *Nrp1*-KO BMDMs (Figures 3A–3C and 3F–3H; Figures S2A and S2B), suggesting that the different distribution of TAMs in LysM-Cre;*Nrp1L^{l}L* mice, not *Nrp1* loss per se, strongly affects their phenotype.

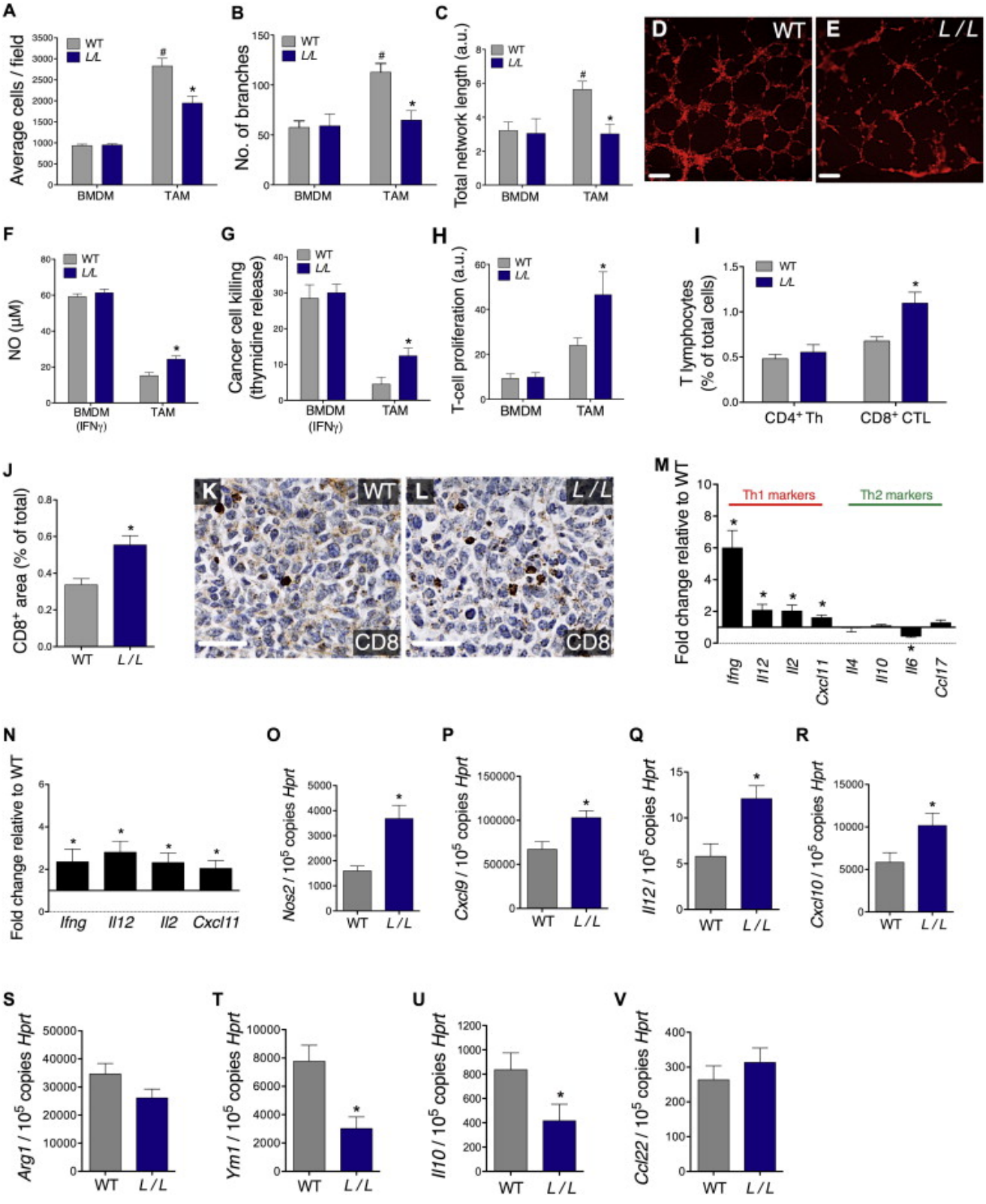

Figure 3.

Exclusion of *Nrp1*-KO TAMs from Hypoxic Areas Prevents Their Angiogenic Phenotype and Restores Their Antitumor Features

(A–E) Histograms showing HUVEC migration toward BMDMs or TAMs isolated from WT or LysM-Cre;*Nrp1L^{l}L* (*L/L*) mice (A), and HUVEC organization (in red), as measured by their branch number (B) and total network length (C) in co-culture with TAMs (D and E).

(F–H) Nitric oxide (NO) release (F), cytotoxicity on thymidine-labeled LLC cancer cells (G), and T cell suppression (H) by BMDMs or TAMs.

(I) FACS quantification on single cell LLC tumor suspensions of CD4$^+$ Th cells and CD8$^+$ cytotoxic T lymphocytes (CTLs).

(J–L) Quantification (J) and micrographs (K and L) of CD8-stained LLC tumor sections.

(M and N) Expression of Th1 (*Ifng*, *Il12*, *Il2*, *Cxcl11*) and Th2 (*Il4*, *Il10*, *Il6*, *Ccl17*) genes in tumor-infiltrating CD4$^+$ Th cells sorted from subcutaneous LLC (M) or PyMT tumors (N) in LysM-Cre;*Nrp1L^{l}L* (*L/L*) mice, normalized to the expressions in WT controls.

(O–V) Expression of the M1 markers *Nos2* (O), *Cxcl9* (P), *Il12* (Q), *Cxcl10* (R), and the M2 markers *Arg1* (S), *Ym1*, (T),*Il10* (U), *Ccl22* (V) in TAMs sorted from subcutaneous LLC tumors.
All experiments, n = 6–12. $^{*}p < 0.05$ versus WT; $^{\#}p < 0.05$ versus BMDMs. Scale bars: 50 μm (D and E) and 25 μm (K and L). All graphs show mean ± SEM. See also Figure S2.

The in vitro effects of *Nrp1*-KO TAMs on ECs are in agreement with the reduced tumor vessel density/area and vascular complexity observed in LysM-Cre;*Nrp1L^{l}L* mice. Because *Nrp1*-KO TAMs also had a milder T cell immunosuppressive capacity, we analyzed how this translated in vivo. The frequency of CD4^{+} T helper cells (Th) in subcutaneous LLC tumors was similar in both genotypes whereas intratumoral CD8^{+} cytotoxic T lymphocytes (CTLs) were 1.6-times more abundant in LysM-Cre;*Nrp1L^{l}L* than in WT mice (Figures 3I–3L). Despite their comparable numbers, CD4^{+} lymphocytes in LysM-Cre;*Nrp1L^{l}L* mice displayed higher expression of antitumoral Th1 markers (Figure 3M). Enhanced CTL recruitment and Th1 T cell skewing, following *Nrp1* loss in myeloid cells, was also observed in PyMT spontaneous breast tumors (Figure 3N). This pronounced Th1/CTL response was associated with an enriched expression of antitumoral M1 genes and decrease of some protumoral M2 markers in TAMs sorted from LysM-Cre;*Nrp1L^{l}L* mice (Figures 3O–3V). However, these genes were equally expressed in cultured WT and *Nrp1*-KO BMDMs, either at baseline (in normoxia or hypoxia) or under forced M1/M2-skewing conditions (Figures S2E–S2L), suggesting that the M1 profile of *Nrp1*-KO TAMs was secondary to microenvironmental changes in the tumor (see below).

When administering anti-CD4 and anti-CD8 antibodies, alone or in combination, depletion of Th cells and/or CTLs in LysM-Cre;*Nrp1L^{l}L* mice mildly (but not significantly) increased growth and weight of subcutaneous LLC tumors compared to tumors treated with an isotype IgG (Figures 4A and 4B). In contrast, depletion of Th cells or CTLs in LysM-Cre;*Nrp1L^{l}L* mice resulted in accelerated LLC tumor growth, reaching comparable sizes as tumors in WT mice (Figures 4A and 4B). Depletion of both CD4^{+} and CD8^{+} T cells had similar effects as depletion of CD8^{+} T cells alone, indicating that CTLs are the main effectors of tumor inhibition in LysM-Cre;*Nrp1L^{l}L* mice (Figures 4A and 4B). The efficiency of intratumoral CD4^{+} cell depletion was almost complete in both WT and LysM-Cre;*Nrp1L^{l}L* mice, and anti-CD8 antibodies did not affect the frequency of Th cells in both genotypes (Figure 4C). Conversely, tumor-infiltrating CTLs were 2.3 times more abundant in LysM-Cre;*Nrp1L^{l}L* versus WT mice, but they were reduced by 40%, 90%, and 96%, respectively, following anti-CD4, anti-CD8, or combined treatment (Figure 4D). Circulating CD4^{+} and CD8^{+} cell numbers did not differ in both WT and LysM-Cre;*Nrp1L^{l}L* mice, and treatment with anti-CD4 and/or anti-CD8 antibodies depleted these cells from the bloodstream almost completely in both genotypes (Figure S3). Reduction of tumor vessel area and density in LysM-Cre;*Nrp1L^{l}L* mice was independent from Th cells and/or CTLs (Figures 4E and 4F). Instead, the excess of M1-like TAMs in LysM-Cre;*Nrp1L^{l}L* mice was abrogated, partly, by Th cell depletion and, completely, by CTL depletion (Figure 4G).

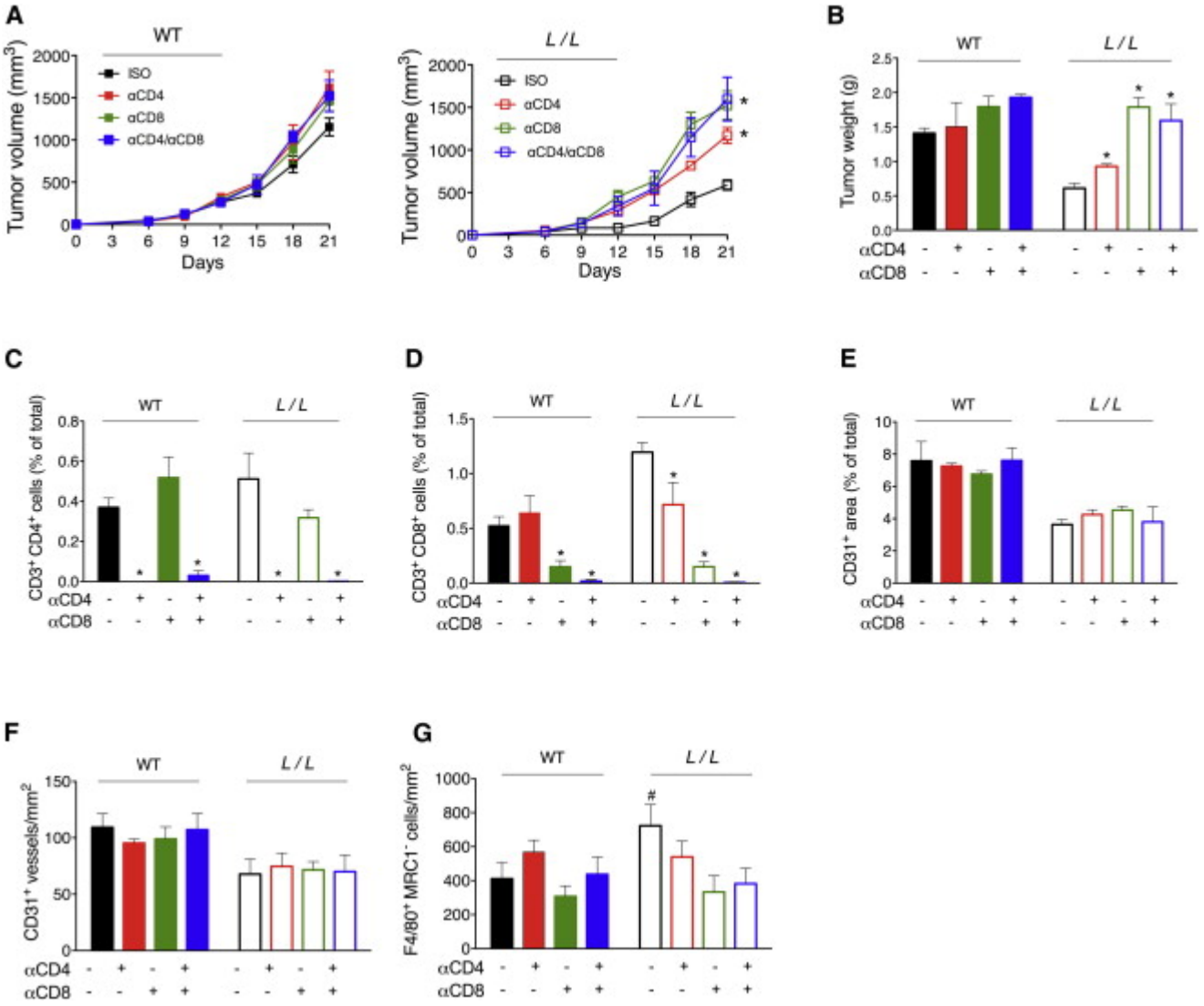

Figure 4.
TAM Redistribution by *Nrp1* Loss Favors T Cell-Mediated Antitumor Immunity
(A and B) Subcutaneous LLC tumor growth in WT (A, left) and LysM-Cre;*Nrp1L*^{l}*L* (*L/L*) mice (A, right), and their end-stage tumor weights (B), following systemic administration of CD4 and CD8 neutralizing antibodies, alone or in combination.
(C and D) Efficiency of Th cell (C) or CTL (D) depletion in the tumors.
(E and F) Quantification of vessel area (E) and vessel density (F) on LLC tumor sections.
(G) Quantification of F4/80^{+}MRC1^{-} M1-like TAM infiltration on LLC tumor sections.
All experiments, n = 6–8. *p < 0.05 versus IgG control. All graphs show mean ± SEM. See also Figure S3.

These data demonstrate that inhibition of TAMs' entry into hypoxic niches hinders their angiogenic and immunosuppressive potential while fostering Th1 cells and CTLs, which, in turn, will sustain macrophage cytotoxicity and adaptive antitumor immunity.

Nrp1 Is Transcriptionally Repressed in Hypoxic Macrophages

Finally, we studied how Nrp1 could be mechanistically involved in TAM positioning inside the hypoxic regions. First, we determined how oxygen tension affects *Nrp1* expression in macrophages. In BMDMs, *Nrp1*transcripts were reduced by 80% in hypoxia compared to normoxia (Figure 5A). Similarly, freshly isolated hypoxic (PIMO-positive) TAMs expressed 90% less *Nrp1* than the normoxic (PIMO-negative) counterpart (Figure 5B). The efficiency of gene deletion was complete in both normoxic and hypoxic BMDMs or TAMs isolated from LysM-Cre;*Nrp1L*^{l}*L* mice (Figures 5A and 5B). Also in tumor sections, Nrp1 was almost undetectable in WT TAMs localized within hypoxic (PIMO-positive) areas; as expected, Nrp1 staining was always negative in TAMs from LysM-Cre;*Nrp1L*^{l}*L* mice (Figure 5C). In contrast, the hypoxia-responsive gene*Flt1* (encoding vascular endothelial growth factor receptor 1 [VEGFR1]) was 5-fold induced in hypoxic versus normoxic BMDMs or TAMs, and *Nrp1* deletion did not affect this regulation (Figures 5D and 5E).

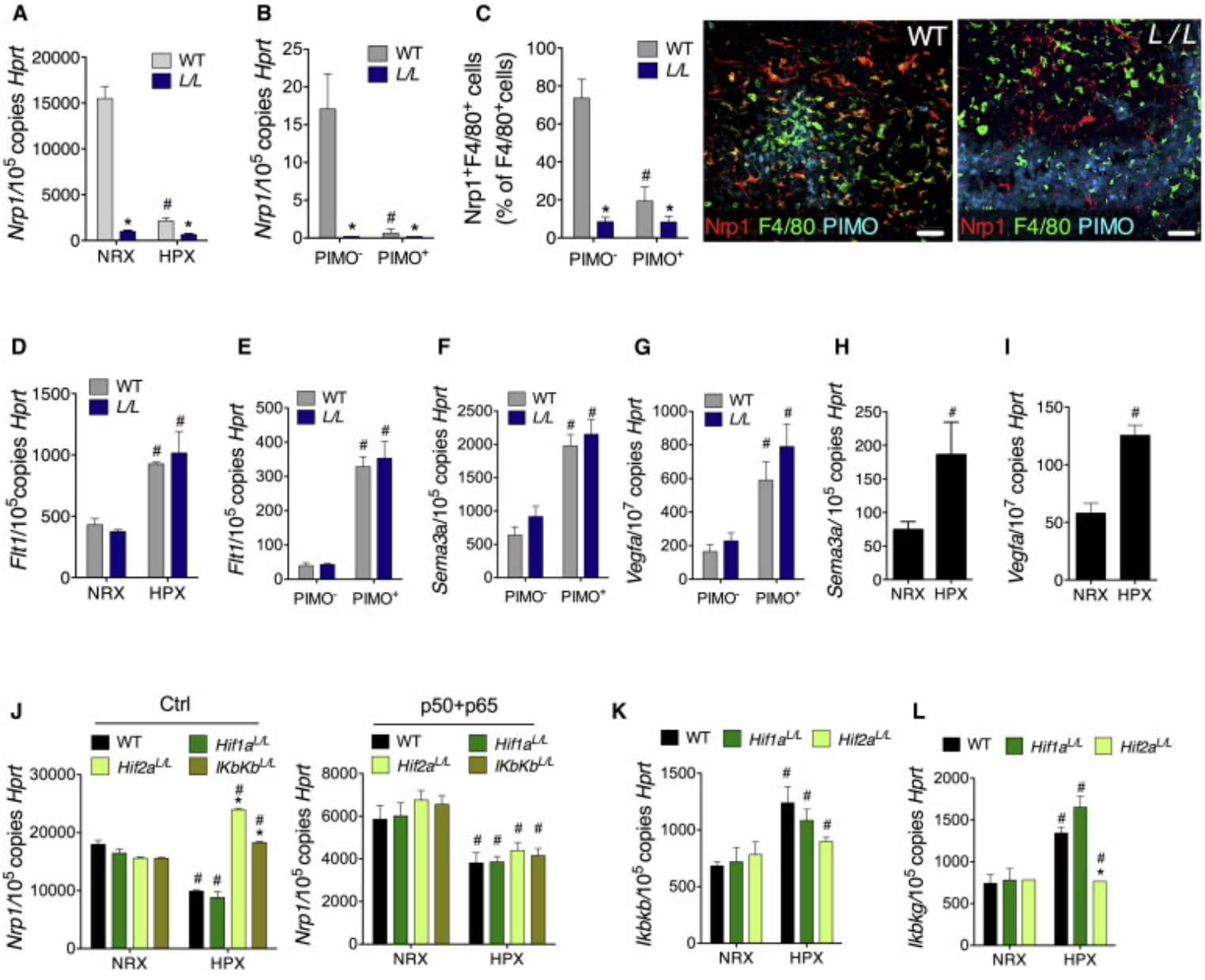

Figure 5.
Hypoxic Repression of *Nrp1* in Macrophages Is Mediated by HIF2-Dependent NF-κB Activity
(A) *Nrp1* expression in BMDMs derived from WT and LysM-Cre;*Nrp1L*^{l}*L* (*L/L*) mice and cultured in normoxia (21% O_2; NRX) or hypoxia (1% O_2; HPX).
(B) *Nrp1* expression in normoxic (PIMO^{-}) or hypoxic (PIMO^{+}) TAMs (E) directly sorted from WT and LysM-Cre;*Nrp1L*^{l}*L*(*L/L*) mice.
(C) Quantification and representative micrographs of Nrp1^{+}F4/80^{+} TAMs in normoxic (PIMO^{-}) or hypoxic (PIMO^{+}) tumor areas.
(D and E) *Flt1* expression in normoxic (NRX) or hypoxic (HPX) BMDMs (D) and in normoxic (PIMO^{-}) or hypoxic (PIMO^{+}) TAMs (E).
(F and G) *Sema3a* (F) or *Vegfa* (G) induction in hypoxic (PIMO^{+}) versus normoxic (PIMO^{-}) tumor cell bulks from either WT or LysM-Cre;*Nrp1L*^{l}*L* (*L/L*) mice.
(H and I) *Sema3a* (H) and *Vegfa* (I) expression in cultured LLC cancer cells.
(J) *Nrp1* transcript levels in WT, *Hif1a*-KO (*Hif1aL/L*), *Hif2a*-KO (*Hif2aL/L*), and *Ikbkb*-KO (*IkbkbL/L*) BMDMs, electroporated with a control (Ctrl) plasmid (on the left) or with two plasmids overexpressing the NF-κB subunits p50 and p65 (on the right), and cultured under normoxic (NRX) or hypoxic (HPX) conditions.
(K and L) *Ikbkb* (K) and *Ikbkg* (L) expression in normoxic (NRX) and hypoxic (HPX) WT, *Hif1a*-KO (*Hif1aL/L*), *Hif2a*-KO (*Hif2aL/L*) BMDMs.
n = 8 in (A–G) and n = 4 in (H–L). $^{*}p < 0.05$ versus WT controls; $^{\#}p < 0.05$ versus NRX or PIMO^{+}. Scale bars: 100 μm. All graphs show mean ± SEM.

We then measured the expression of *Sema3a* and *Vegfa* in hypoxic (PIMO-positive) and normoxic (PIMO-negative) tumor single cell suspensions that contain cancer cells and stromal cells. Both genes were upregulated in the hypoxic fraction of the tumor (Figures 5F and 5G). Consistently, both *Sema3a* and *Vegfa*were induced in LLC cancer cells cultured in hypoxia (1% O_2; Figures 5H and 5I).

When seeking the molecular mechanisms underlying hypoxic repression of *Nrp1* in macrophages, we found that gene deletion of *Hif2a* but not *Hif1a* completely abrogated this downregulation (Figure 5J). In particular, HIF-2 only was entirely responsible for the hypoxic induction of *Ikbkg* and, in good part, of *Ikbkb*, together forming the IKK complex, required for the activation of the canonical NF-κB pathway (Figures 5K and 5L), which can repress *Nrp1* (Hayashi et al., 2012). Indeed, genetic inactivation of this pathway in *Ikbkb*-KO macrophages prevented *Nrp1* downregulation by hypoxia; overexpression of p50/p65 NF-κB subunits in*Hif2a*-KO or *Ikbkb*-KO macrophages restored this transcriptional repression (Figure 5J). These data indicate that hypoxic stabilization of HIF-2 in macrophages unleashes the canonical NF-κB pathway via IKK induction. Consequently, release of active p50/p65 heterodimers blocks *Nrp1* expression.

Nrp1 Regulation by Hypoxia Defines Macrophage Responses to Sema3A

Prompted by the above observations, we assessed the chemotactic potential of Sema3A or VEGF on WT and *Nrp1*-KO macrophages, isolated respectively from WT and LysM-Cre;*Nrp1L*^{l}*L* mice. In the presence of Sema3A, migration of WT BMDMs was doubled whereas *Nrp1*-KO BMDMs did not respond. $VEGF_{164}$ was equally potent but the absence of *Nrp1* decreased this migratory response by only 30%. Thus, Nrp1 is strictly necessary for macrophage attraction by Sema3A, but not by $VEGF_{164}$. Indeed, $VEGF_{120}$ (which does not bind Nrp1 effectively; Soker et al., 1998) was as good as $VEGF_{164}$ in attracting both WT and *Nrp1*-KO BMDMs (Figure 6A). In line with the migratory phenotype, Sema3A and $VEGF_{164}$ induced cytoskeleton remodeling and macrophage elongation; however, while the absence of *Nrp1* completely abrogated Sema3A activity, it marginally reduced the response to $VEGF_{164}$ (Figure S4A).

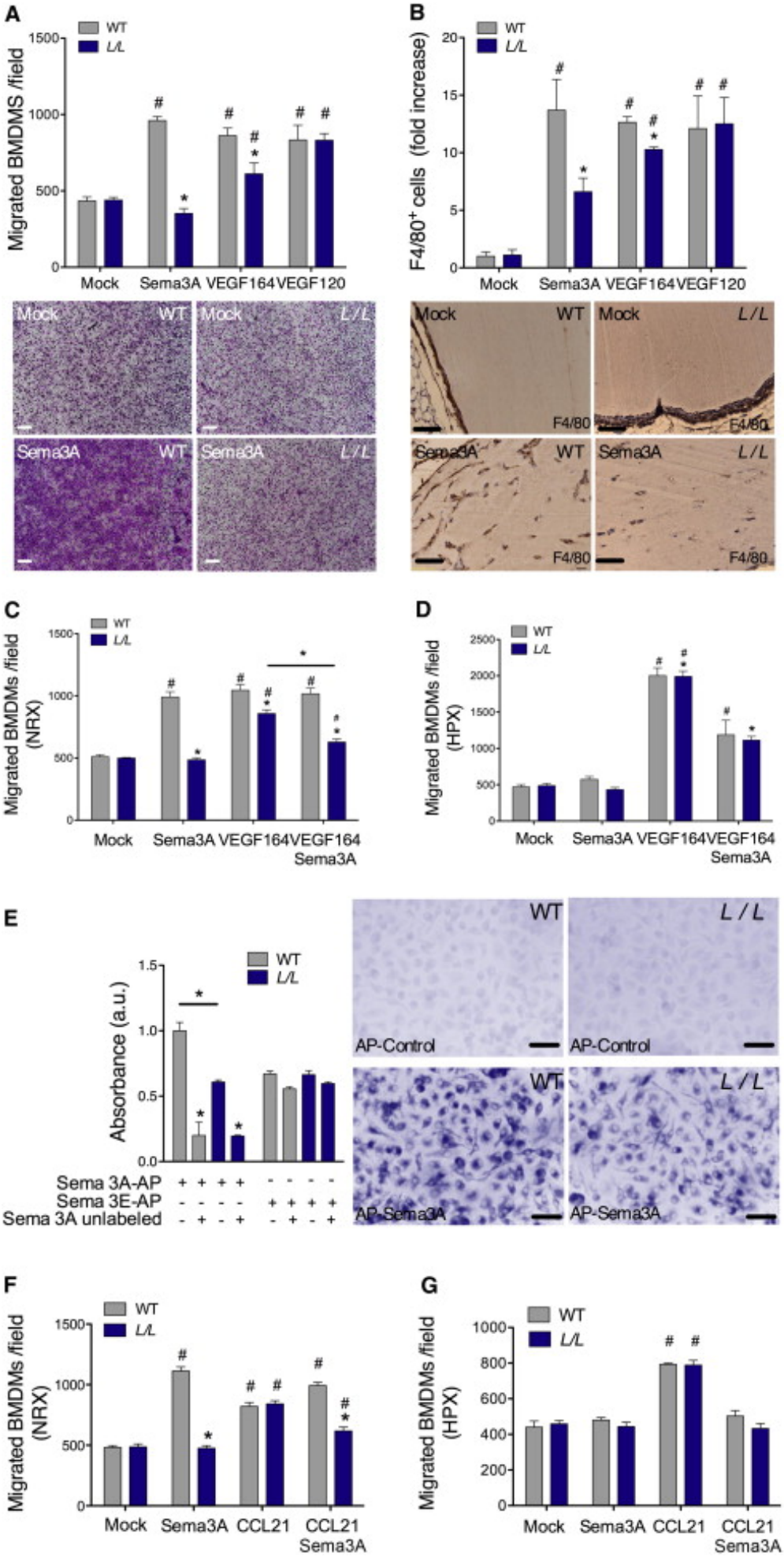
A
Migrated BMDMS /field
WT
L/L
Mock
Sema3A
VEGF164
VEGF120
Mock WT
Mock L/L
Sema3A WT
Sema3A L/L
B
F4/80+ cells (fold increase)
F4/80
C
Migrated BMDMs /field (NRX)
VEGF164 Sema3A
D
Migrated BMDMs /field (HPX)
E
Absorbance (a.u.)
Sema 3A-AP
Sema 3E-AP
Sema 3A unlabeled
AP-Control
AP-Sema3A
F
CCL21
CCL21 Sema3A
G

Figure 6.
Sema3A Attracts or Retains Macrophages Depending on the Presence or Absence of Nrp1
(A) Migration of WT and *Nrp1*-KO (*L/L*) BMDMs toward Sema3A, $VEGF_{164}$, or $VEGF_{120}$.
(B) Migration of $F4/80^+$ macrophages in subcutaneous matrigel plugs supplemented with Sema3A, $VEGF_{164}$, or $VEGF_{120}$.
(C and D) Migration of WT and *Nrp1*-KO (*L/L*) BMDMs toward Sema3A and $VEGF_{164}$, alone or in combination, under normoxic (NRX; C) or hypoxic (HPX; D) conditions.
(E) Binding of Sema3A-AP (or Sema3E-AP as control) to WT and *Nrp1*-KO (*L/L*) BMDMs in absence or presence of 2-fold molar excess of unlabeled Sema3A. Cell-bound AP activity was revealed in situ using colorimetric reactions as shows in micrographs.
(F and G) Migration of WT and *Nrp1*-KO (*L/L*) BMDMs toward Sema3A and $VEGF_{164}$, alone or in combination, under normoxic (NRX; F) or hypoxic (HPX; G) conditions.
$^*p < 0.05$ versus WT; $^\#p < 0.05$ versus mock. Scale bars: 100 μm in (A), 50 μm in (B), and 20 μm in (E). All graphs show mean ± SEM of four independent experiments. See also Figure S4.

Similar results were obtained in vivo, where subcutaneous matrigel plugs containing recombinant Sema3A, $VEGF_{164}$, or $VEGF_{120}$ displayed a strong and comparable macrophage infiltration. Loss of *Nrp1* reduced macrophage attraction to Sema3A by 50% and to $VEGF_{164}$ by 20% only, whereas $VEGF_{120}$ activity did not change (Figure 6B).

Because Sema3A and $VEGF_{164}$ are present together in the tumor and are both induced by hypoxia, we assessed in vitro macrophage migration in response to combined Sema3A and $VEGF_{164}$ under either normoxia or hypoxia (1% O_2). Interestingly, in normoxia, this combination did not further increase the migration of WT macrophages compared to either cytokine alone, whereas *Nrp1*-KO macrophages further lost their migratory response to VEGF (Figure 6C). In hypoxia, neither WT nor *Nrp1*-KO macrophages were attracted toward Sema3A (consistent with hypoxia-mediated and genetic-driven *Nrp1* loss, respectively); conversely, their response to $VEGF_{164}$ was even stronger than in normoxia (Figure 6D), likely because of hypoxia-mediated VEGFR1 induction. However, the migration of hypoxic macrophages (either WT or *Nrp1*-KO) was barely induced upon combined stimulation with Sema3A and $VEGF_{164}$ (Figure 6D).

These data suggest a Nrp1-independent function of Sema3A antagonizing VEGF-induced attraction and prompted our search for evidence that Sema3A can interact with macrophages even in the absence of Nrp1. Cell-binding experiments in situ with alkaline-phoshatase (AP) tagged molecules demonstrated that Sema3A binding is also remarkably present on *Nrp1*-KO cells (about 50% less than in WT cells), as validated by specific competition by unlabeled Sema3A (Figure 6E). Thus, Sema3A can specifically interact with *Nrp1*-KO macrophages, potentially accounting for the functional activity observed in hypoxic conditions.

The chemokine CCL21 can elicit macrophage egression from tumor hypoxic niches because its levels are much higher in normoxic versus hypoxic cancer cells (Figure S4B). Remarkably, Sema3A significantly reduced the migration toward CCL21 of *Nrp1*-KO or hypoxic WT macrophages, where *Nrp1* is also barely detectable (Figures 6F and 6G). These data further support the conclusion that, while Sema3A attracts macrophages in a Nrp1-dependent manner, it is still active and can convey a migration-inhibitory effect upon Nrp1 downregulation in the same cells.

Sema3A Activates Opposite Signaling in Presence or Absence of Nrp1

Semaphorins are mainly known as repelling signals, acting through receptors called plexins. However, when plexins transactivate receptor tyrosine kinases (RTKs), semaphorin signals can be converted into attractive cues (Tamagnone, 2012). At least in one case, this was found to implicate the expression of Nrp1 (Bellon et al., 2010). While studying Sema3A-mediated activation of RTKs in macrophages, we found that Sema3A induced VEGFR1 Tyr1213 phosphorylation more potently than $VEGF_{164}$ itself. Loss of *Nrp1* in macrophages completely abrogated Sema3A-dependent VEGFR1 activation without significantly affecting the response to VEGF (Figures 7A and 7B).

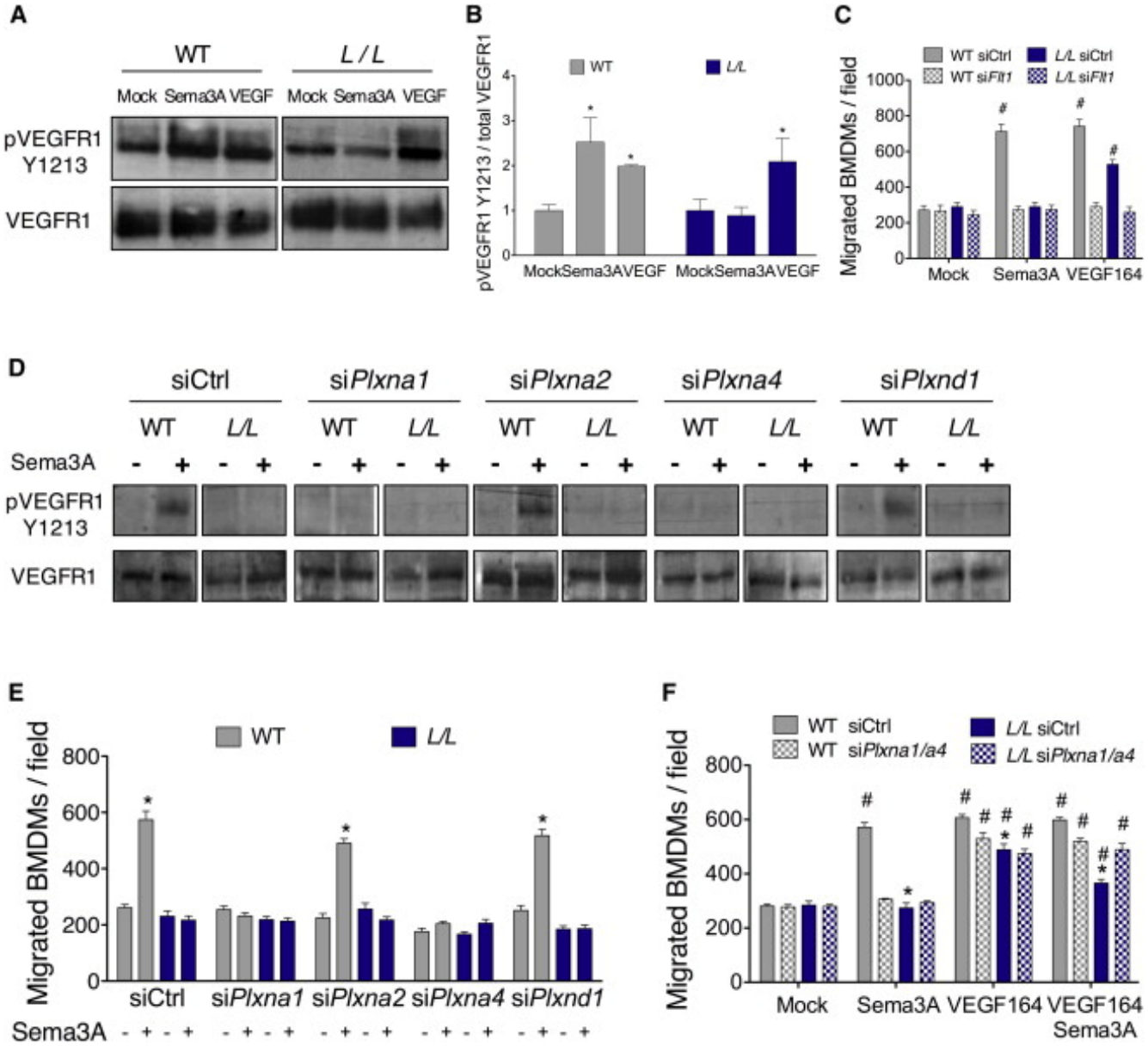

Figure 7.

TAM Attraction by Sema3A Involves VEGFR1, whereas Their Retention Requires PlexinA1/A4 Only

(A and B) Western blot (A) and densitometry (B) for VEGFR1 Y1213 phosphorylation in WT and *Nrp1*-KO (*L/L*) BMDMs upon Sema3A and VEGF stimulation.

(C) Migration toward Sema3A or $VEGF_{164}$ of WT and *Nrp1*-KO (*L/L*) BMDMs silenced for *Flt1* (si*Flt1*) or scramble control (shCtrl).

(D and E) VEGFR1 phosphorylation (D) and migration (E) in Sema3A-treated WT and *Nrp1*-KO (*L/L*) BMDMs, upon silencing of *Plxna1*, *Plxna2, Plxna4*, or *Plxnd1*.

(F) Migration of WT and *Nrp1*-KO (*L/L*) BMDMs toward Sema3A and $VEGF_{164}$, alone or together, upon combined silencing of *Plxna1* and *Plxna4*.

*$p < 0.05$ versus WT; #$p < 0.05$ versus mock. All graphs show mean ± SEM of three to four independent experiments. See also Figure S5.

We then knocked down VEGFR1 in both WT and *Nrp1*-KO BMDMs (Figure S5A) and assessed the biological consequences on Sema3A-mediated migration. Whereas Nrp1 was largely dispensable for the migratory response toward $VEGF_{164}$, the knockdown of VEGFR1 entirely prevented the migration of both WT and *Nrp1*-KO macrophages in response to either Sema3A or $VEGF_{164}$. This suggested that Nrp1 requires VEGFR1 to transduce Sema3A-mediated attractive signals, whereas VEGFR1 alone can mediate VEGF activity in macrophages (Figure 7C).

We then evaluated the expression of plexins known to form semaphorin holoreceptors in association with Nrp1, namely PlexinA1, PlexinA2, PlexinA3, PlexinA4, and PlexinD1 (Tamagnone, 2012). All these plexins,

except PlexinA3, were detectable in TAMs and BMDMs and equally expressed in both WT and *Nrp1*-KO cells (Figures S5B and S5C). Silencing of PlexinA1 or PlexinA4 (but not of PlexinA2 or PlexinD1) in WT BMDMs (Figure S5D) abrogated Sema3A-mediated VEGFR1 phosphorylation and migration as potently as genetic deletion of *Nrp1* (Figures 7D and 7E). These cells were still migrating in response to serum stimulation, confirming their viability (Figures S5E and S5F).

Moreover, upon costimulation with Sema3A and VEGF, silencing of PlexinA1 and PlexinA4 prevented the migratory blockade orchestrated by Sema3A in *Nrp1*-KO BMDMs (Figure 7F). Thus, in presence of Nrp1, a Sema3A/PlexinA1/PlexinA4 axis mediates attractive cues via VEGFR1 transactivation, which are reverted into stop signals in the absence of Nrp1.

Sema3A Defines TAM Positioning within the Tumor

To assess the specific role of Sema3A in vivo, we used two complementary strategies. First, we used*Nrp1*$^{Sema-}$ knock-in (KI) mice, which have a disrupted Sema3A-Nrp1 binding site that leaves $VEGF_{165}$-Nrp1 binding unaffected (Gu et al., 2003). As expected, *Nrp1*$^{Sema-}$ macrophages did not migrate toward Sema3A whereas they responded normally to either $VEGF_{164}$ or $VEGF_{120}$ (Figure 8A). Compared to control mice (WT→WT), WT recipient mice transplanted with bone marrow (BM) cells from *Nrp1*$^{Sema-}$ mice (KI→WT) displayed tumor growth inhibition and decreased vessel area and density, accompanied by increased tumor hypoxia and macrophage infiltration (Figures 8B–8G). Importantly, *Nrp1*$^{Sema-}$ TAMs failed to enter hypoxic tumor regions, thus resembling the overall phenotype observed in tumor-bearing LysM-Cre;*Nrp1L*^{l}*L* mice (Figure 8H).

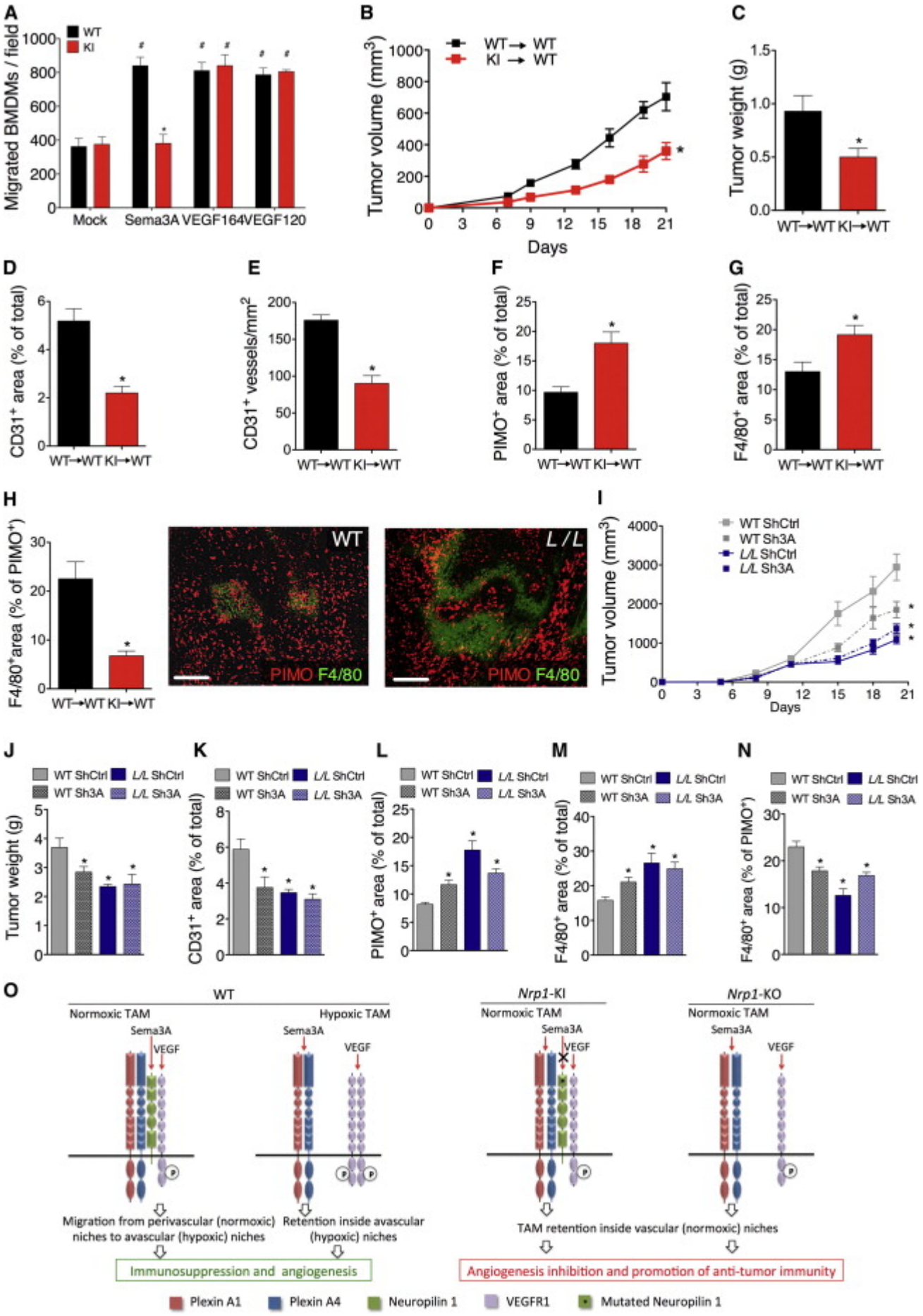
A
Migrated BMDMs / field
WT
KI
Mock
Sema3A
VEGF164
VEGF120
B
Tumor volume (mm3)
WT → WT
KI → WT
Days
C
Tumor weight (g)
WT→WT KI→WT
D
CD31+ area (% of total)
E
CD31+ vessels/mm2
F
PIMO+ area (% of total)
G
F4/80+ area (% of total)
H
F4/80+area (% of PIMO+)
WT
L/L
PIMO F4/80
I
Tumor volume (mm3)
WT ShCtrl
WT Sh3A
L/L ShCtrl
L/L Sh3A
Days
J
Tumor weight (g)
K
CD31+ area (% of total)
L
PIMO+ area (% of total)
M
F4/80+ area (% of total)
N
F4/80+ area (% of PIMO+)
O
WT
Normoxic TAM
Hypoxic TAM
Nrp1-KI
Nrp1-KO
Sema3A
VEGF
Migration from perivascular (normoxic) niches to avascular (hypoxic) niches
Retention inside avascular (hypoxic) niches
TAM retention inside vascular (normoxic) niches
Immunosuppression and angiogenesis
Angiogenesis inhibition and promotion of anti-tumor immunity
Plexin A1
Plexin A4
Neuropilin 1
VEGFR1
Mutated Neuropilin 1

Figure 8.
Sema3A Defines TAM Positioning within the Tumor
(A) Migration of WT and *Nrp1*$^{Sema-}$ (KI) BMDMs in response to Sema3A, $VEGF_{164}$, or $VEGF_{120}$.
(B and C) Growth (B) and weight (C) of subcutaneous LLC tumors injected in mice transplanted with BM from WT or*Nrp1*$^{Sema-}$ mice (WT→WT and KI→WT, respectively).
(D–F) Tumor vessel area (D), tumor vessel density (E), and tumor hypoxia (F) in WT→WT and KI→WT mice.
(G) Histological quantification of $F4/80^+$ TAM accumulation in WT→WT and KI→WT mice.
(H) Quantification and micrographs showing $F4/80^+$ TAMs in $PIMO^+$ hypoxic tumor regions.
(I–N) Growth (I), weight (J), $CD31^+$ vessel area (K), $PIMO^+$ hypoxic area (L), total $F480^+$ TAM accumulation (M), and hypoxic TAM accumulation (N) in tumors derived from Sema3A-silenced LLC (Sh3A) or from scramble control LLC (ShCtrl), injected subcutaneously in WT and LysM-Cre;*Nrp1L*^{l}*L* (*L*/*L*) mice.
(O) VEGF and Sema3A attract TAMs from peri-vascular (normoxic) areas to avascular (hypoxic) niches through VEGFR1 transactivation. While VEGF works independently of Nrp1, Sema3A-mediated VEGFR1 activation requires Nrp1 as well as PlexinA1 and PlexinA4. Upon repression of Nrp1 by hypoxia, Sema3A retains TAMs inside the hypoxic niche through PlexinaA1/A4 signaling. Hypoxic TAMs acquire an immunosuppressive and pro-angiogenic phenotype, which contributes to tumor growth and metastasis. Because of loss of Sema3A binding to Nrp1 in *Nrp1*$^{Sema-}$ (KI) TAMs or gene deletion in*Nrp1*-KO TAMs, Sema3A does not attract but rather entraps TAMs in the perivascular (normoxic) areas countering attraction by VEGF or other cytokines in a PlexinA1/A4-dependent manner. Normoxic TAMs are then less angiogenic and more antitumoral.
n = 4 in (A), n = 10 in (B–H), and n = 6–8 in (I–N). $^{*}p < 0.05$ versus WT; $^{\#}p < 0.05$ versus mock. Scale bars: 100 μm. All graphs show mean ± SEM. See also Figure S6.

Second, we established subcutaneous tumors by injection of Sema3A-silenced LLC (LLC-Sh3A) or scrambled controls (LLC-ShCtrl) in WT and LysM-Cre;*Nrp1L*^{l}*L* mice. *Sema3*a knockdown was 85% in normoxia and completely prevented hypoxic induction of *Sema3a* (Figure S6A). In vitro proliferation of LLC-Sh3A and LLC-ShCtrl was comparable (Figure S6B). However, LLC-Sh3A tumors in WT mice displayed growth and vessel inhibition, as well as TAM exclusion from hypoxic areas, to a similar extent as LLC-ShCtrl tumors in LysM-Cre;*Nrp1L*^{l}*L* mice. Yet, Sema3A silencing did not further affect these parameters in LysM-Cre;*Nrp1L*^{l}*L* mice (Figures 8I–8N). All these data indicate that cancer cell-derived Sema3A, not VEGF, is responsible for TAM entry into hypoxic niches through Nrp1 signaling.

Discussion

Several hypotheses have proposed how TAMs might be recruited to and retained in the hypoxic tumor microenvironment, including hypoxia-mediated upregulation of chemoattractants and downregulation of chemokine receptors (Murdoch and Lewis, 2005). We describe a mechanism whereby Nrp1 in macrophages is dispensable for their recruitment from the bloodstream but necessary for TAM positioning in hypoxic niches. Because macrophages differentiate from extravasated circulating monocytes, TAMs will initially accumulate in the proximity of the vascularized and perfused niche. From there, they will then move toward avascular/hypoxic areas of the tumor where they presumably clear necrotic cell debris. We now show that hypoxia upregulates Sema3A and VEGF, and these signals act as macrophage attractants by inducing, respectively, Nrp1-dependent or Nrp1-independent VEGFR1 transactivation (Figure 8O). Once macrophages localize in the hypoxic area, Nrp1 expression in TAMs is downregulated terminating their migratory response to Sema3A, and therefore they remain entrapped on site. Notably, TAMs expressing a Nrp1 mutant that cannot bind Sema3A (but that still retains its ability to bind VEGF) fail to enter the hypoxic regions of the tumor similarly to *Nrp1*-KO TAMs. These data indicate that VEGF signaling is not sufficient to drive TAM localization into hypoxic areas and support the idea of the presence of inhibitory signals able to blunt TAM attraction by VEGF and other factors (such as CCL21). We found that Sema3A itself can play such a role upon downregulation of Nrp1 expression in TAMs by mediating plexin-dependent stop signals. Further work will define if the mechanism proposed by our study holds true in other pathologies. For instance, Nrp1 in macrophages is not required for developmental angiogenesis (not shown and Fantin et al., 2013), likely because the expression of its ligand Sema3A starts later during embryogenesis (Püschel et al., 1995).

Whereas Nrp1 has been considered a major component of the Sema3A receptor complex in association with plexins, we report an Nrp1-independent specific binding of Sema3A to macrophages, deploying inhibition of chemotactic signaling via PlexinA1/A4 effectors. X-ray crystallographic analyses demonstrated that Sema3A carries the same structural features enabling other semaphorins to directly interact with plexins and trigger their inhibitory signals (Janssen et al., 2012 and Nogi et al., 2010). However, this association seems to require

the stabilizer function of additional ligand-binding components, commonly identified in Nrp1. In the absence of Nrp1, Sema3A binding is reduced but not abrogated, consistent with our observations in macrophages. Previous reports illustrated the interaction between Sema3A and chondroitin-sulfate glycosaminoglycans on the plasma membrane (De Wit et al., 2005). The punctate distribution of these molecules at the cell surface is indeed reminiscent of that observed for Sema3A bound to neuronal cells (De Wit et al., 2005) and, in our study, to macrophages. This may suggest a role for proteoglycans in Sema3A receptor complexes found in macrophages, in association with plexins, similar to what is known for other cell guidance cues and soluble factors (de Wit and Verhaagen, 2007 and Fuster and Esko, 2005).

TAMs in avascular/hypoxic areas represent a deadly combination because TAMs respond to hypoxia with an altered gene expression profile leading to the development of a distinct protumoral phenotype that favors angiogenesis, metastasis, and suppresses antitumor immune responses (Burke et al., 2003, Doedens et al., 2010 and Movahedi et al., 2010). Here, we formally prove that accumulation of TAMs in normoxic regions and their exclusion from hypoxic tumor regions (upon loss of *Nrp1*) blunt their angiogenic and immunosuppressive capacity, resulting in reduced vessel branching and Th1/CTL-mediated antitumor immune responses. The release of cytokines, such as interferon gamma (IFNγ), by Th1 T cells and especially by CTL will polarize the newly recruited TAMs in M1-like cytotoxic macrophages, thus initiating a feed-forward loop that enhances antitumor immunity (Biswas and Mantovani, 2010, Coussens et al., 2013 and Johansson et al., 2008). Reduced angiogenesis and tumor perfusion will also initiate a feed-forward loop because the resulting hypoxia will lead to more TAM recruitment (Eltzschig and Carmeliet, 2011 and Murdoch and Lewis, 2005). Nevertheless, these TAMs will not enter the hypoxic niches because of lack of Nrp1, and this will perpetuate their antitumor phenotype. These findings might explain some observations in human tumor biopsies where higher numbers of TAMs do not always correlate with a worse prognosis but rather with a favorable disease outcome or the clinical correlation between different TAM localizations and patient survival (De Palma and Lewis, 2013).

Different from what occurs in macrophages, Sema3A-mediated Nrp1 signaling acts as a restrictive signal for EC migration (Serini et al., 2003) and exogenous delivery of Sema3A in tumor models can inhibit angiogenesis and hinder tumor growth (Casazza et al., 2011, Maione et al., 2009 and Maione et al., 2012). Notably, in these previous studies, TAM distribution into tumors had not been tested. Moreover, while guidance cues such as Sema3A are known to organize cell migration and neurite extension in a topographically controlled manner, their exogenous delivery into tissues may elicit pharmacological effects overwhelming the functional complexity of the endogenous signals. Indeed, the formation of a vascular network is a dynamic process that depends on pro-angiogenic and anti-angiogenic stimuli (Mazzone et al., 2009). Once recruited to the tumor from the bloodstream, TAMs will be attracted from perivascular/normoxic into avascular/hypoxic niches by Sema3A via an Nrp1/PlexinA1/A4/VEGFR1 signaling platform. Downregulation of Nrp1 arrests TAMs in their position through Nrp1-independent Sema3A-mediated PlexinA1/A4 signals. Here, TAMs secrete “angiokines” such as VEGF and Sema3A, and matrix metalloproteases including MMP2 and MMP9 (Movahedi et al., 2010, Murdoch and Lewis, 2005 and Pucci et al., 2009). ECs will thus follow the macrophages into the hypoxic regions of the tumor, where they are attracted by VEGF, but their migration will be partly limited by Sema3A-repelling signals, as Nrp1 expression in ECs is induced by hypoxia, in contrast to macrophages (Ottino et al., 2004 and Zhang et al., 2001). Future studies will elucidate how *Nrp1* is inversely regulated by hypoxia in different cellular contexts. The reported ability of Sema3A-Nrp1 signaling to guide TAM migration into hypoxic niches, where they eventually are entrapped, is reminiscent of the activity of axonal guidance cues featuring navigation “go” and “stop” signals at distinctive sites, depending on the level of signaling components (Guthrie, 1999, Nawabi et al., 2010 and Schwarz and Ruhrberg, 2010). To prove the functional relevance of this specific mechanism in vivo, we selectively inhibited Sema3A binding to Nrp1 in macrophages or we silenced Sema3A in cancer cells, and found that, consistent with preventing TAM migration into hypoxic niches, this reduced angiogenesis and tumor growth. Overall, our results and the previous works show that localized activity of endogenous Sema3A in individual cell populations versus pharmacological administration of exogenous Sema3A can have divergent effects on tumor growth in vivo. Interestingly, antibodies selectively

blocking Sema3A binding to Nrp1, despite their scarce activity on ECs in vitro, inhibit angiogenesis and vessel remodeling in vivo with a similar efficacy as antibodies blocking VEGF binding to Nrp1, thus possibly implying the effective blockade of other pro-angiogenic cells such as macrophages (Pan et al., 2007).

Consistent with the finding that Sema3A can mediate attractive or repulsive cues, its expression has been associated with both tumor progression (Biankin et al., 2012 and Müller et al., 2007) and tumor suppression (Maione et al., 2009 and Yacoub et al., 2009); however the functional relevance of the endogenous molecule in adult tissues has not been fully elucidated. Our study sheds light on the role of Sema3A/Nrp1 signaling in the guidance of macrophages into hypoxic niches. Thus, Sema3A expression in tumors may also predict the ability to drive TAMs toward hypoxic niches to escape antitumor immunity and to promote vascularization.

Experimental Procedures
More detailed methods can be found in the Supplemental Experimental Procedures.

Tumor Models
LLC cells were injected subcutaneously (2×10^6 cells) or orthotopically (1×10^6 cells); Panc02 was injected into the tail of the pancreas (1 ± 10^6 cells). PyMT tumors were classified as before (Lin et al., 2003). All mouse procedures were approved by the Institutional Animal Care and Research Advisory Committee of the K.U. Leuven.

BM Transplantation
Lethally irradiated C56BL/6 mice (9.5 Gy) were intravenously injected with 10^7 BM cells from *Nrp1*$^{Sema-}$mice. Tumor experiments were initiated 6 weeks after BM reconstitution.

Western Blot and Immunochemistry
Protein extraction was performed using extraction buffer (20 mM Tris HCl, 150 mM NaCl, 1% Triton X-100, 10% glycerol, and 5 mM EDTA). Immunostaining protocols and hypoxia detection were performed as before (Mazzone et al., 2009). Tumor perfusion was assessed with intravenous injection of 0.05 mg lectin-FITC.

FACS Analysis and Flow Sorting of Tumor-Associated Cells
LLC subcutaneous tumors were minced in RPMI medium containing 0.1% collagenase type I and 0.2% dispase type I (30 min at 37°C), passed through a 19 G needle, and filtered. After RBC lysis, cells were resuspended in fluorescence-activated cell sorting buffer (PBS containing 2% fetal bovine serum and 2 mM EDTA) and incubated with Mouse BD Fc Block purified antimouse CD16/CD32 mAb (BD PharMingen), followed by staining with anti-F4/80, CD3, CD4, CD8, CD115, Ly6C, Ly6G, CD11c, CD11b, and MRC1 for 20 min at 4°C. F4/80$^+$ TAMs were sorted from subcutaneous LLC tumors; hypoxic TAMs were sorted as before (Movahedi et al., 2010).

Migration Assays
Six-week-old mice were subcutaneously injected with 500 µl of growth factor-reduced Matrigel (BD Biosciences), supplemented with either PBS or with 1 µg purified murine Sema3A, $VEGF_{164}$, or $VEGF_{120}$(R&D). After 5 days, mice were sacrificed and macrophage recruitment was evaluated by histological analysis. Skin inflammation was induced by ear painting with the phorbol ester TPA and analyzed after 24 hr.

Endothelial Cell Capillary Formation
Sorted TAMs or 10^5 BMDMs were embedded in growth factor-reduced Matrigel (BD Biosciences). After 36 hr, 10^4 human umbilical vein endothelial cells (HUVECs) fluorescently labeled with PKH-26 (Sigma-Aldrich) were added to the Matrigel. Alternatively, a conditioned medium (obtained from 2.5×10^5 BMDMs or sorted TAMs in culture for 36 hr) was used to resuspend 10^4 HUVECs, which were then seeded directly on Matrigel. After 4 hr, capillary formation was analyzed by measuring the number of branches and length of the vascular network using ImageJ software.

Macrophage Cytotoxicity Assay

LLC cells were labeled with 1 μCi/ml ^{3}H-Thymidine for 20 hr. Then, 10^{4} cells were seeded together with increasing concentrations of activated BMDMs (20 ng/ml IFNγ + 100 ng/ml lipopolysaccharide for 24 hr) or sorted TAMs. After 24 hr, LLC cell death was detected by measuring radioactivity in a cell-free medium.

T Cell Suppression

For T cell suppression, 2×10^{5} naive C57BL/6 splenocytes were added to increasing concentrations of BMDMs or sorted TAMs, and stimulated with 1 μg/ml anti-CD3. After 24 hr, cells were pulsed with ^{3}H-thymidine (PerkinElmer) and incubated for another 18 hr before incorporated radioactivity was measured.

T Cell Depletion

Th-cell and CTL depletion was performed in LLC tumor-bearing mice with intraperitoneal injection of 0.2 mg anti-CD4 (GK1.5) or anti-CD8 (53-6.7; BioXCell), respectively, or rat IgG isotypes as control, every third day, starting the sixth day after tumor injection.

Statistics

Data indicate mean ± SEM of representative experiments. Statistical significance was calculated by two-tailed unpaired t test for two data sets (or Chi-square for PyMT tumor staging and Gehan-Breslow-Wilcoxon for the survival upon orthotopic LLC tumor implantation), with $p < 0.05$ considered as statistically significant.

Acknowledgments

The authors thank J. Serneels, Y. Jonsson, and Y. Elkrim for technical assistance and Dr. Serini, Dr. Carmeliet, and Dr. De Palma for comments. M.M. was supported by an ERC starting grant, L.T. by AIRC-IG no.11-598 and MIUR-PRIN grants, A.C. by EMBO, and D.L. by VLK. *Nrp1L/L* and *Nrp1*$^{Sema-}$ mice were a gift of Dr. Gu (Harvard University) and Dr. Ginty (Johns Hopkins); the iCSF1R-Cre line was provided by Dr. Pollard (Albert Einstein College of Medicine).

References

A. Bellon, J. Luchino, K. Haigh, G. Rougon, J. Haigh, S. Chauvet, F. Mann
VEGFR2 (KDR/Flk1) signaling mediates axon growth in response to semaphorin 3E in the developing brain. Neuron, 66 (2010), pp. 205–219

A.V. Biankin, N. Waddell, K.S. Kassahn, M.C. Gingras, L.B. Muthuswamy, A.L. Johns, D.K. Miller, P.J. Wilson, A.M. Patch, J. Wu, Australian Pancreatic Cancer Genome Initiative*et al.*
Pancreatic cancer genomes reveal aberrations in axon guidance pathway genes. Nature, 491 (2012), pp. 399–405

S.K. Biswas, A. Mantovani
Macrophage plasticity and interaction with lymphocyte subsets: cancer as a paradigm. Nat. Immunol., 11 (2010), pp. 889–896

B. Blouw, H. Song, T. Tihan, J. Bosze, N. Ferrara, H.P. Gerber, R.S. Johnson, G. Bergers
The hypoxic response of tumors is dependent on their microenvironment. Cancer Cell, 4 (2003), pp. 133–146

D. Bruder, M. Probst-Kepper, A.M. Westendorf, R. Geffers, S. Beissert, K. Loser, H. von Boehmer, J. Buer, W. Hansen
Neuropilin-1: a surface marker of regulatory T cells. Eur. J. Immunol., 34 (2004), pp. 623–630

B. Burke, A. Giannoudis, K.P. Corke, D. Gill, M. Wells, L. Ziegler-Heitbrock, C.E. Lewis
Hypoxia-induced gene expression in human macrophages: implications for ischemic tissues and hypoxia-regulated gene therapy. Am. J. Pathol., 163 (2003), pp. 1233–1243

A. Casazza, X. Fu, I. Johansson, L. Capparuccia, F. Andersson, A. Giustacchini, M.L. Squadrito, M.A. Venneri, M. Mazzone, E. Larsson *et al.*
Systemic and targeted delivery of semaphorin 3A inhibits tumor angiogenesis and progression in mouse tumor models. Arterioscler. Thromb. Vasc. Biol., 31 (2011), pp. 741–749

A. Catalano
The neuroimmune semaphorin-3A reduces inflammation and progression of experimental autoimmune arthritis. J. Immunol., 185 (2010), pp. 6373–6383

A. Catalano, P. Caprari, S. Moretti, M. Faronato, L. Tamagnone, A. Procopio
Semaphorin-3A is expressed by tumor cells and alters T-cell signal transduction and function. Blood, 107 (2006), pp. 3321–3329

L.M. Coussens, L. Zitvogel, A.K. Palucka
Neutralizing tumor-promoting chronic inflammation: a magic bullet? Science, 339 (2013), pp. 286–291

M. De Palma, C.E. Lewis
Macrophage regulation of tumor responses to anticancer therapies. Cancer Cell, 23 (2013), pp. 277–286

J. de Wit, J. Verhaagen
Proteoglycans as modulators of axon guidance cue function. Adv. Exp. Med. Biol., 600 (2007), pp. 73–89

J. De Wit, F. De Winter, J. Klooster, J. Verhaagen
Semaphorin 3A displays a punctate distribution on the surface of neuronal cells and interacts with proteoglycans in the extracellular matrix. Mol. Cell. Neurosci., 29 (2005), pp. 40–55

G.M. Delgoffe, S.R. Woo, M.E. Turnis, D.M. Gravano, C. Guy, A.E. Overacre, M.L. Bettini, P. Vogel, D. Finkelstein, J. Bonnevier *et al.*
Stability and function of regulatory T cells is maintained by a neuropilin-1-semaphorin-4a axis. Nature, 501 (2013), pp. 252–256

A.L. Doedens, C. Stockmann, M.P. Rubinstein, D. Liao, N. Zhang, D.G. DeNardo, L.M. Coussens, M. Karin, A.W. Goldrath, R.S. Johnson
Macrophage expression of hypoxia-inducible factor-1 alpha suppresses T-cell function and promotes tumor progression. Cancer Res., 70 (2010), pp. 7465–7475

H.K. Eltzschig, P. Carmeliet
Hypoxia and inflammation. N. Engl. J. Med., 364 (2011), pp. 656–665

A. Fantin, J.M. Vieira, G. Gestri, L. Denti, Q. Schwarz, S. Prykhozhij, F. Peri, S.W. Wilson, C. Ruhrberg
Tissue macrophages act as cellular chaperones for vascular anastomosis downstream of VEGF-mediated endothelial tip cell induction. Blood, 116 (2010), pp. 829–840

A. Fantin, J.M. Vieira, A. Plein, L. Denti, M. Fruttiger, J.W. Pollard, C. Ruhrberg
NRP1 acts cell autonomously in endothelium to promote tip cell function during sprouting angiogenesis. Blood, 121 (2013), pp. 2352–2362

M.M. Fuster, J.D. Esko
The sweet and sour of cancer: glycans as novel therapeutic targets. Nat. Rev. Cancer, 5 (2005), pp. 526–542

H. Gerhardt, C. Ruhrberg, A. Abramsson, H. Fujisawa, D. Shima, C. Betsholtz
Neuropilin-1 is required for endothelial tip cell guidance in the developing central nervous system. Dev. Dyn., 231 (2004), pp. 503–509

C. Gu, E.R. Rodriguez, D.V. Reimert, T. Shu, B. Fritzsch, L.J. Richards, A.L. Kolodkin, D.D. Ginty
Neuropilin-1 conveys semaphorin and VEGF signaling during neural and cardiovascular development. Dev. Cell, 5 (2003), pp. 45–57

S. Guthrie
Axon guidance: starting and stopping with slit. Curr. Biol., 9 (1999), pp. R432–R435

W. Hansen, M. Hutzler, S. Abel, C. Alter, C. Stockmann, S. Kliche, J. Albert, T. Sparwasser, S. Sakaguchi, A.M. Westendorf *et al.*
Neuropilin 1 deficiency on $CD4^{+}Foxp3^{+}$ regulatory T cells impairs mouse melanoma growth. J. Exp. Med., 209 (2012), pp. 2001–2016

M. Hayashi, T. Nakashima, M. Taniguchi, T. Kodama, A. Kumanogoh, H. Takayanagi
Osteoprotection by semaphorin 3A. Nature, 485 (2012), pp. 69–74

T.M. Hong, Y.L. Chen, Y.Y. Wu, A. Yuan, Y.C. Chao, Y.C. Chung, M.H. Wu, S.C. Yang, S.H. Pan, J.Y. Shih *et al.* Targeting neuropilin 1 as an antitumor strategy in lung cancer. Clin. Cancer Res., 13 (2007), pp. 4759–4768

B.J. Janssen, T. Malinauskas, G.A. Weir, M.Z. Cader, C. Siebold, E.Y. Jones
Neuropilins lock secreted semaphorins onto plexins in a ternary signaling complex. Nat. Struct. Mol. Biol., 19 (2012), pp. 1293–1299

M. Johansson, D.G. Denardo, L.M. Coussens
Polarized immune responses differentially regulate cancer development. Immunol. Rev., 222 (2008), pp. 145–154

A.L. Kolodkin, D.V. Levengood, E.G. Rowe, Y.T. Tai, R.J. Giger, D.D. Ginty
Neuropilin is a semaphorin III receptor. Cell, 90 (1997), pp. 753–762

W.C. Liang, M.S. Dennis, S. Stawicki, Y. Chanthery, Q. Pan, Y. Chen, C. Eigenbrot, J. Yin, A.W. Koch, X. Wu *et al.*
Function blocking antibodies to neuropilin-1 generated from a designed human synthetic antibody phage library. J. Mol. Biol., 366 (2007), pp. 815–829

E.Y. Lin, J.G. Jones, P. Li, L. Zhu, K.D. Whitney, W.J. Muller, J.W. Pollard
Progression to malignancy in the polyoma middle T oncoprotein mouse breast cancer model provides a reliable model for human diseases. Am. J. Pathol., 163 (2003), pp. 2113–2126

F. Maione, F. Molla, C. Meda, R. Latini, L. Zentilin, M. Giacca, G. Seano, G. Serini, F. Bussolino, E. Giraudo
Semaphorin 3A is an endogenous angiogenesis inhibitor that blocks tumor growth and normalizes tumor vasculature in transgenic mouse models. J. Clin. Invest., 119 (2009), pp. 3356–3372

F. Maione, S. Capano, D. Regano, L. Zentilin, M. Giacca, O. Casanovas, F. Bussolino, G. Serini, E. Giraudo
Semaphorin 3A overcomes cancer hypoxia and metastatic dissemination induced by antiangiogenic treatment in mice. J. Clin. Invest., 122 (2012), pp. 1832–1848

M. Mazzone, D. Dettori, R. Leite de Oliveira, S. Loges, T. Schmidt, B. Jonckx, Y.M. Tian, A.A. Lanahan, P. Pollard, C. Ruiz de Almodovar *et al.*
Heterozygous deficiency of PHD2 restores tumor oxygenation and inhibits metastasis via endothelial normalization. Cell, 136 (2009), pp. 839–851

K. Movahedi, D. Laoui, C. Gysemans, M. Baeten, G. Stangé, J. Van den Bossche, M. Mack, D. Pipeleers, P. In't Veld, P. De Baetselier, J.A. Van Ginderachter
Different tumor microenvironments contain functionally distinct subsets of macrophages derived from Ly6C(high) monocytes. Cancer Res., 70 (2010), pp. 5728–5739

M.W. Müller, N.A. Giese, J.M. Swiercz, G.O. Ceyhan, I. Esposito, U. Hinz, P. Büchler, T. Giese, M.W. Büchler, S. Offermanns, H. Friess
Association of axon guidance factor semaphorin 3A with poor outcome in pancreatic cancer. Int. J. Cancer, 121 (2007), pp. 2421–2433

C. Murdoch, C.E. Lewis
Macrophage migration and gene expression in response to tumor hypoxia. Int. J. Cancer, 117 (2005), pp. 701–708

H. Nawabi, A. Briançon-Marjollet, C. Clark, I. Sanyas, H. Takamatsu, T. Okuno, A. Kumanogoh, M. Bozon, K. Takeshima, Y. Yoshida *et al.*
A midline switch of receptor processing regulates commissural axon guidance in vertebrates. Genes Dev., 24 (2010), pp. 396–410

M. Niedergethmann, R. Hildenbrand, B. Wostbrock, M. Hartel, J.W. Sturm, A. Richter, S. Post
High expression of vascular endothelial growth factor predicts early recurrence and poor prognosis after curative resection for ductal adenocarcinoma of the pancreas. Pancreas, 25 (2002), pp. 122–129

T. Nogi, N. Yasui, E. Mihara, Y. Matsunaga, M. Noda, N. Yamashita, T. Toyofuku, S. Uchiyama, Y. Goshima, A. Kumanogoh, J. Takagi
Structural basis for semaphorin signalling through the plexin receptor. Nature, 467 (2010), pp. 1123–1127

P. Ottino, J. Finley, E. Rojo, A. Ottlecz, G.N. Lambrou, H.E. Bazan, N.G. Bazan
Hypoxia activates matrix metalloproteinase expression and the VEGF system in monkey choroid-retinal endothelial cells: Involvement of cytosolic phospholipase A2 activity. Mol. Vis., 10 (2004), pp. 341–350

Q. Pan, Y. Chanthery, W.C. Liang, S. Stawicki, J. Mak, N. Rathore, R.K. Tong, J. Kowalski, S.F. Yee, G. Pacheco *et al.*
Blocking neuropilin-1 function has an additive effect with anti-VEGF to inhibit tumor growth. Cancer Cell, 11 (2007), pp. 53–67

F. Pucci, M.A. Venneri, D. Biziato, A. Nonis, D. Moi, A. Sica, C. Di Serio, L. Naldini, M. De Palma
A distinguishing gene signature shared by tumor-infiltrating Tie2-expressing monocytes, blood "resident" monocytes, and embryonic macrophages suggests common functions and developmental relationships. Blood, 114 (2009), pp. 901–914

A.W. Püschel, R.H. Adams, H. Betz
Murine semaphorin D/collapsin is a member of a diverse gene family and creates domains inhibitory for axonal extension. Neuron, 14 (1995), pp. 941–948

B.Z. Qian, J. Li, H. Zhang, T. Kitamura, J. Zhang, L.R. Campion, E.A. Kaiser, L.A. Snyder, J.W. Pollard
CCL2 recruits inflammatory monocytes to facilitate breast-tumour metastasis. Nature, 475 (2011), pp. 222–225

C. Rolny, M. Mazzone, S. Tugues, D. Laoui, I. Johansson, C. Coulon, M.L. Squadrito, I. Segura, X. Li, E. Knevels *et al.*
HRG inhibits tumor growth and metastasis by inducing macrophage polarization and vessel normalization through downregulation of PlGF. Cancer Cell, 19 (2011), pp. 31–44

Q. Schwarz, C. Ruhrberg
Neuropilin, you gotta let me know: should I stay or should I go? Cell Adhes. Migr., 4 (2010), pp. 61–66

G. Serini, D. Valdembri, S. Zanivan, G. Morterra, C. Burkhardt, F. Caccavari, L. Zammataro, L. Primo, L. Tamagnone, M. Logan *et al.*
Class 3 semaphorins control vascular morphogenesis by inhibiting integrin function. Nature, 424 (2003), pp. 391–397

S. Soker, S. Takashima, H.Q. Miao, G. Neufeld, M. Klagsbrun
Neuropilin-1 is expressed by endothelial and tumor cells as an isoform-specific receptor for vascular endothelial growth factor. Cell, 92 (1998), pp. 735–745

H. Takamatsu, N. Takegahara, Y. Nakagawa, M. Tomura, M. Taniguchi, R.H. Friedel, H. Rayburn, M. Tessier-Lavigne, Y. Yoshida, T. Okuno *et al.*
Semaphorins guide the entry of dendritic cells into the lymphatics by activating myosin II. Nat. Immunol., 11 (2010), pp. 594–600

Y. Takeda, S. Costa, E. Delamarre, C. Roncal, R. Leite de Oliveira, M.L. Squadrito, V. Finisguerra, S. Deschoemaeker, F. Bruyère, M. Wenes *et al.*
Macrophage skewing by Phd2 haplodeficiency prevents ischaemia by inducing arteriogenesis. Nature, 479 (2011), pp. 122–126

L. Tamagnone
Emerging role of semaphorins as major regulatory signals and potential therapeutic targets in cancer. Cancer Cell, 22 (2012), pp. 145–152

R. Tordjman, Y. Lepelletier, V. Lemarchandel, M. Cambot, P. Gaulard, O. Hermine, P.H. Roméo
A neuronal receptor, neuropilin-1, is essential for the initiation of the primary immune response. Nat. Immunol., 3 (2002), pp. 477–482

M. Yacoub, A. Coulon, O. Celhay, J. Irani, O. Cussenot, G. Fromont
Differential expression of the semaphorin 3A pathway in prostatic cancer. Histopathology, 55 (2009), pp. 392–398

Z.G. Zhang, W. Tsang, L. Zhang, C. Powers, M. Chopp
Up-regulation of neuropilin-1 in neovasculature after focal cerebral ischemia in the adult rat. J. Cereb. Blood Flow Metab., 21 (2001), pp. 541–549

Cancer Cell, Volume *24*

Supplemental Information

Impeding Macrophage Entry into Hypoxic Tumor Areas by Sema3A/Nrp1 Signaling Blockade Inhibits Angiogenesis and Restores Antitumor Immunity

Andrea Casazza, Damya Laoui, Mathias Wenes, Sabrina Rizzolio, Nicklas Bassani, Marco Mambretti, Sofie Deschoemaeker, Jo A. Van Ginderachter, Luca Tamagnone, and Massimiliano Mazzone

SUPPLEMENTAL DATA

TABLE S1, RELATED TO FIGURE 1.

	Parameter	WT	*L/L*
Tumor-free mice	WBC	4.73 ± 0.49	4.55 ± 0.36
	NEU	15.01 ± 1.46	15.66 ± 2.13
	LYM	77.76 ± 1.90	78.29 ± 2.00
	MON	2.24 ± 0.17	2.15 ± 0.26
	EOS	2.09 ± 0.48	1.62 ± 0.33
	BAS	2.74 ± 0.13	2.30 ± 0.23
	RBC (M/μl)	6.76 ± 0.40	6.55 ± 0.52
	HGB (g/dl)	9.81 ± 0.62	9.11 ± 0.86
	HCT (%)	52.60 ± 3.39	48.90 ± 4.70
	MCHC (g/dl)	18.64 ± 0.08	18.61 ± 0.07
	PLT (K/μl)	645.25 ± 58.47	365.36 ± 26.28
Tumor-bearing mice	WBC	7.18 ± 0.42	7.25 ± 0.51
	NEU	33.84 ± 4.06	26.39 ± 2.75
	LYM	56.43 ± 4.27	64.10 ± 3.54
	MON	4.19 ± 0.61	3.75 ± 0.62
	EOS	1.99 ± 0.37	2.21 ± 0.43
	BAS	3.53 ± 0.18	3.45 ± 0.27
	RBC (M/μl)	6.95 ± 0.12	6.41 ± 0.31
	HGB (g/dl)	8.88 ± 0.37	8.08 ± 0.19
	HCT (%)	53.55 ± 1.06	51.77 ± 1.37
	MCHC (g/dl)	18.60 ± 0.07	18.61 ± 0.06
	PLT (K/μl)	757.50 ± 38.80	768.50 ± 55.68

The values represent hematological parameters (mean ± SEM) in control (LysM-Cre;*Nrp1*$^{+/+}$; WT in short) and myeloid cell-specific *Nrp1*-KO mice (LysM-Cre;*Nrp1*$^{L/L}$; *L/L* in short), measured before (tumor-free) and 14 days after the implantation of subcutaneous LLC tumors (tumor-bearing). n=18. Abbreviations: white blood cell (WBC), neutrophil (NEU), lymphocyte (LYM), monocyte (MON), eosinophil (EOS), basophil (BAS), red blood cell (RBC), hemoglobin (HGB), hematocrit (HCT), mean cell hemoglobin concentration (MCHC), platelet (PLT).

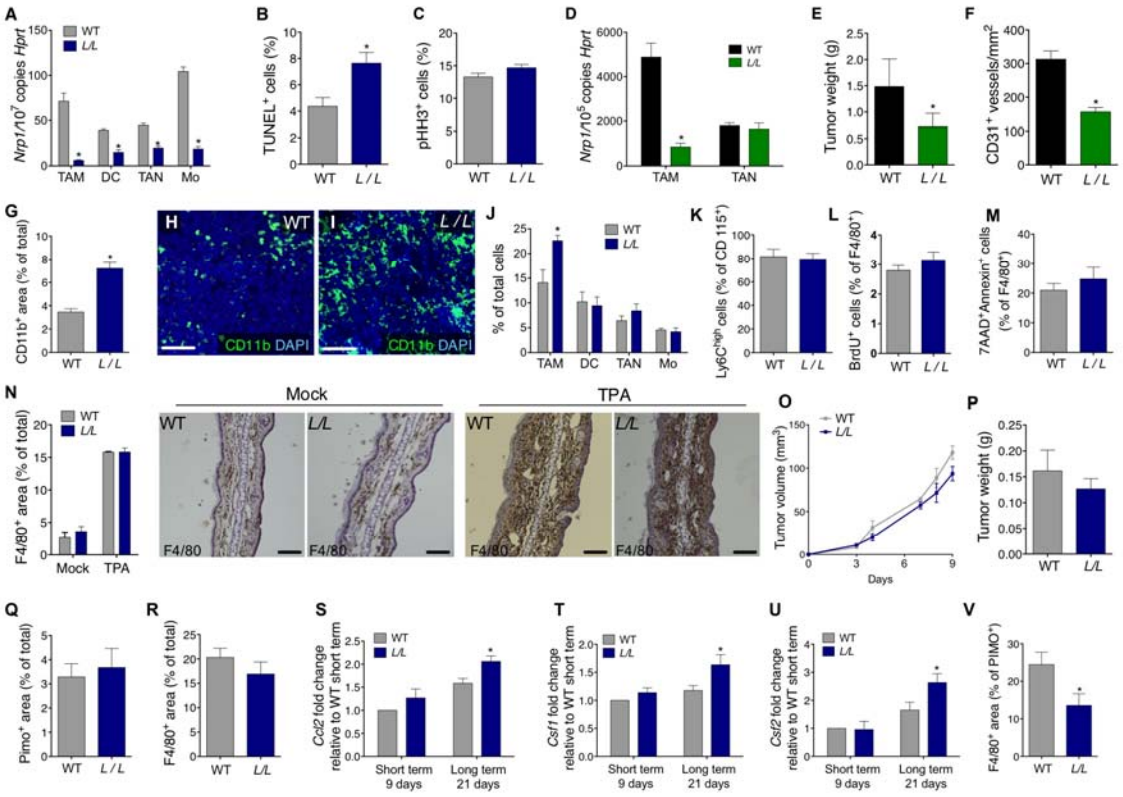

FIGURE S1, RELATED TO FIGURE 1.

(A) *Nrp1* RNA levels in tumor-associated macrophages (TAM), dendritic cells (DC), tumor-associated neutrophils (TAN), and circulating monocytes (Mo), sorted from WT and LysM-Cre;$Nrp1^{L/L}$ (*L/L*) mice, subcutaneously implanted with LLC tumors. n=5. (**B,C)** Quantification of apoptosis (B) by TUNEL staining and proliferation (C) by anti-phosphohistone H3 (pHH3) staining, on thin sections from subcutaneous LLC tumors in WT and LysM-Cre;$Nrp1^{L/L}$ (*L/L*) mice. n=8. **(D)** *Nrp1* RNA levels in TAM and TAN, sorted from subcutaneous LLC tumors implanted shortly after tamoxifen administration in iCSF1R-Cre;$Nrp1^{+/+}$ (WT) and iCSF1R-Cre;$Nrp1^{L/L}$ (*L/L*) mice. n=4. **(E,F)** Weight (E) and vessel density (F) of subcutaneous LLC tumors implanted shortly after tamoxifen administration in WT and iCSF1R-Cre;$Nrp1^{L/L}$ (*L/L*) mice. n=5. **(G-I)** Quantification (G) and representative micrographs (H,I) of LLC tumor sections stained for the myeloid cell marker CD11b in WT and LysM-Cre;$Nrp1^{L/L}$ (*L/L*) mice. n=8. **(J)** FACS analysis on different myeloid cell populations showing the density of tumor-

associated macrophages (TAM), dendritic cells (DC), tumor-associated neutrophils (TAN) and circulating monocytes (Mo) in WT and LysM-Cre;*Nrp1*$^{L/L}$ (*L/L*) mice, subcutaneously implanted with LLC tumors. n=8-12. **(K)** Fractions of circulating Ly6^{high} inflammatory monocytes in both genotypes as analyzed by FACS. n=8-12. **(L,M)** Fraction of apoptotic (7AAD^{+}Annexin^{+}) TAMs (L) or proliferating (BrdU^{+}) TAMs (M) as analyzed by FACS. n=8-12. **(N)** Quantification and staining for F4/80, at baseline (mock) and 24 hr after cutaneous application of TPA on the ear of WT and LysM-Cre;*Nrp1*$^{L/L}$ (*L/L*) mice. n=10. **(O-R)** Growth (O), weight (P), hypoxia (Q), and total TAM infiltration (R) 9 days after subcutaneous LLC tumor implantation in WT and LysM-Cre;*Nrp1*$^{L/L}$ (*L/L*) mice. n=12. **(S-U)** RNA levels of *Ccl2* (S), *Csf1* (T), and *Csf2* (U) in LLC subcutaneous tumors at short term (9 days post-implantation; n=4) and long term (21 days post-implantation; n=5) in WT and LysM-Cre;*Nrp1*$^{L/L}$ (*L/L*) mice. **(V)** TAM infiltration of PIMO^{+} hypoxic areas in subcutaneous LLC tumors at short term. n=12. *$p<0.05$ versus WT; $^{\#}p<0.05$ versus normoxia (NRX). Scale bars: 100 μm. All graphs show mean ± SEM.

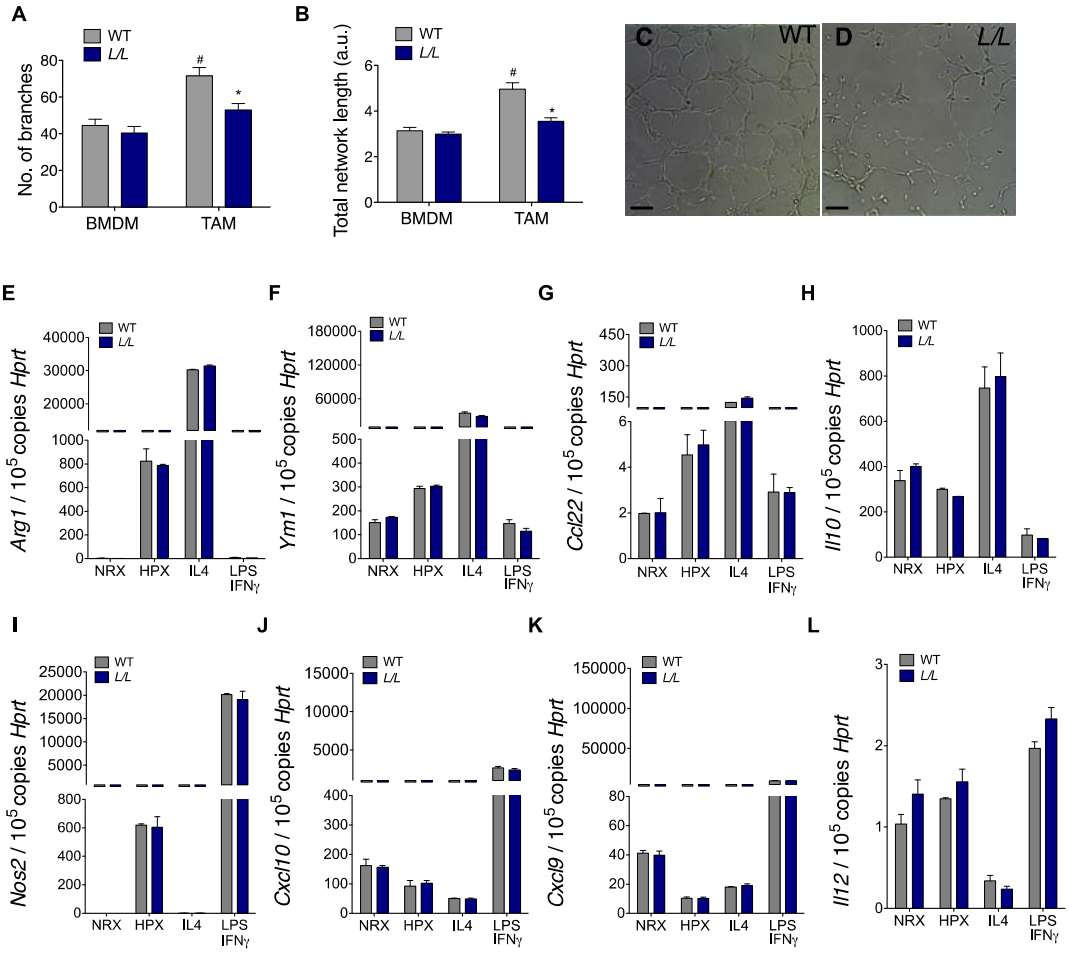

FIGURE S2, RELATED TO FIGURE 3.

(A-D) Number of branches (A) and total network length (B) of HUVEC upon stimulation with soluble factors contained in the conditioned media from WT and *Nrp1*-KO BMDMs or TAMs, isolated respectively from WT and LysM-Cre;*Nrp1*$^{L/L}$ (*L/L*) mice; representative images of HUVEC stimulated with TAM-conditioned media are shown in C and D. n=3-4. **(E-L)** RNA levels of the M2 markers *Arg1* (E), *Ym1* (F), *Ccl22* (G), *Il10* (H), and the M1 markers *Nos2* (I), *Cxcl10* (J), *Cxcl9* (K), *Il12* (L) in WT and *Nrp1*-KO BMDMs, isolated respectively from WT and LysM-Cre;*Nrp1*$^{L/L}$ (*L/L*) mice and cultured under normoxia (NRX; 21% O_2), hypoxia (1% O_2; HPX), M2-skewing IL4, or M1-skewing LPS + IFNγ. n=5. *p<0.05 versus WT; $^{\#}$p<0.05 versus BMDMs. Scale bars: 50μm. All graphs show mean ± SEM.

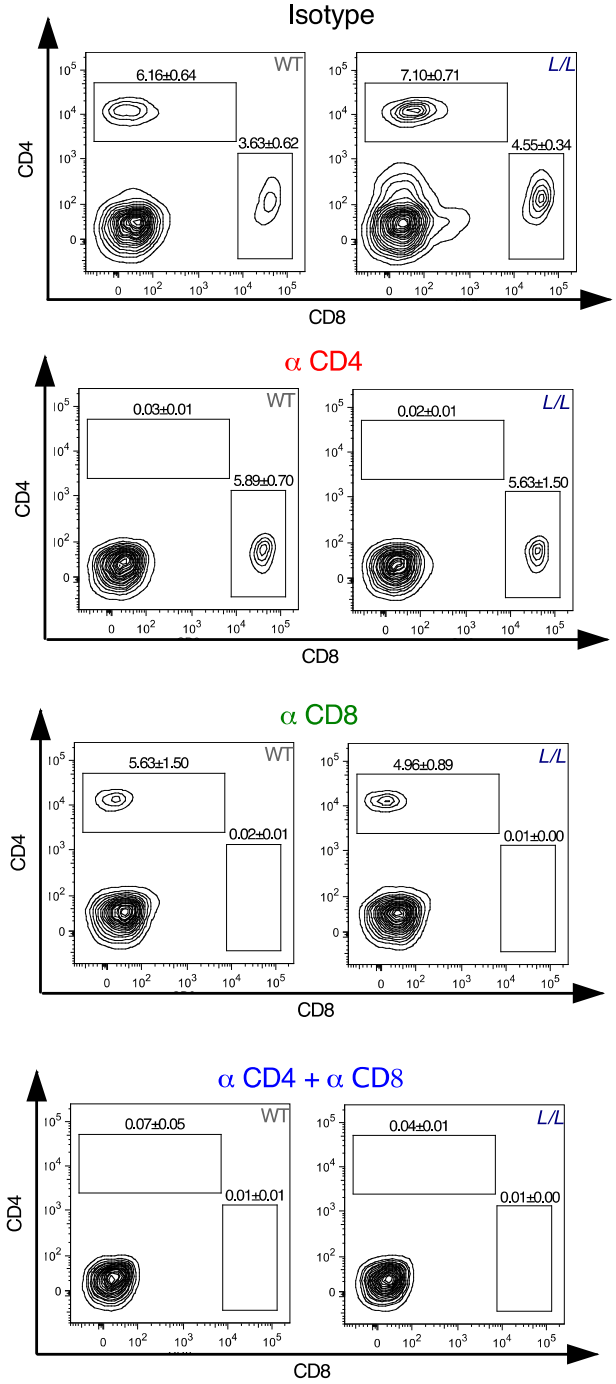

FIGURE S3, RELATED TO FIGURE 4.

FACS plots showing the percentage of circulating $CD4^+$ and $CD8^+$ cells, out of the $CD3^+$ population, in subcutaneous LLC tumor-bearing WT and LysM-Cre;*Nrp1*$^{L/L}$ (*L/L*) mice upon treatment with CD4 and/or CD8 neutralizing antibodies. n=6. All values represent mean ± SEM.

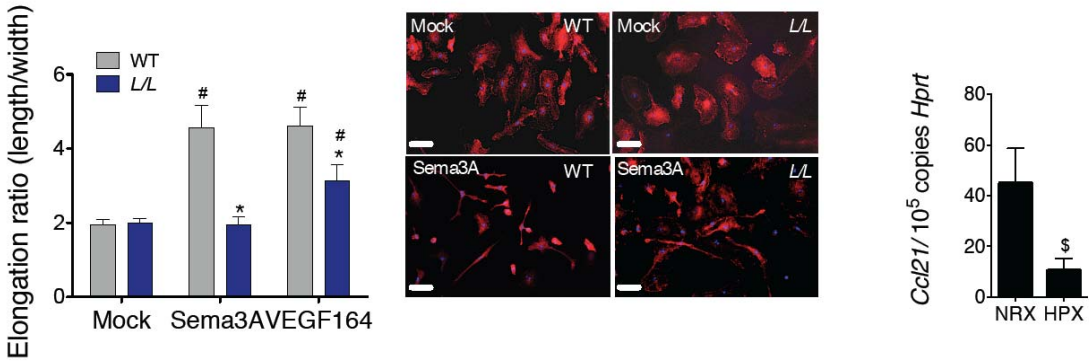

FIGURE S4, RELATED TO FIGURE 6.

(A) Elongation of WT and *Nrp1*-KO (*L/L*) BMDMs upon Sema3A stimulation as shown by phalloidin staining; DAPI was used as nuclear marker. n=2. **(B)** RNA levels of *Ccl21* in LLC cancer cells exposed to normoxia (NRX; 21% O_2) or hypoxia (HPX; 1% O_2). n=3. *p<0.05 versus WT; $^{\#}$p<0.05 versus mock; $^{\$}$p<0.05 versus NRX. Scale bars: 50μm. All graphs show mean ± SEM.

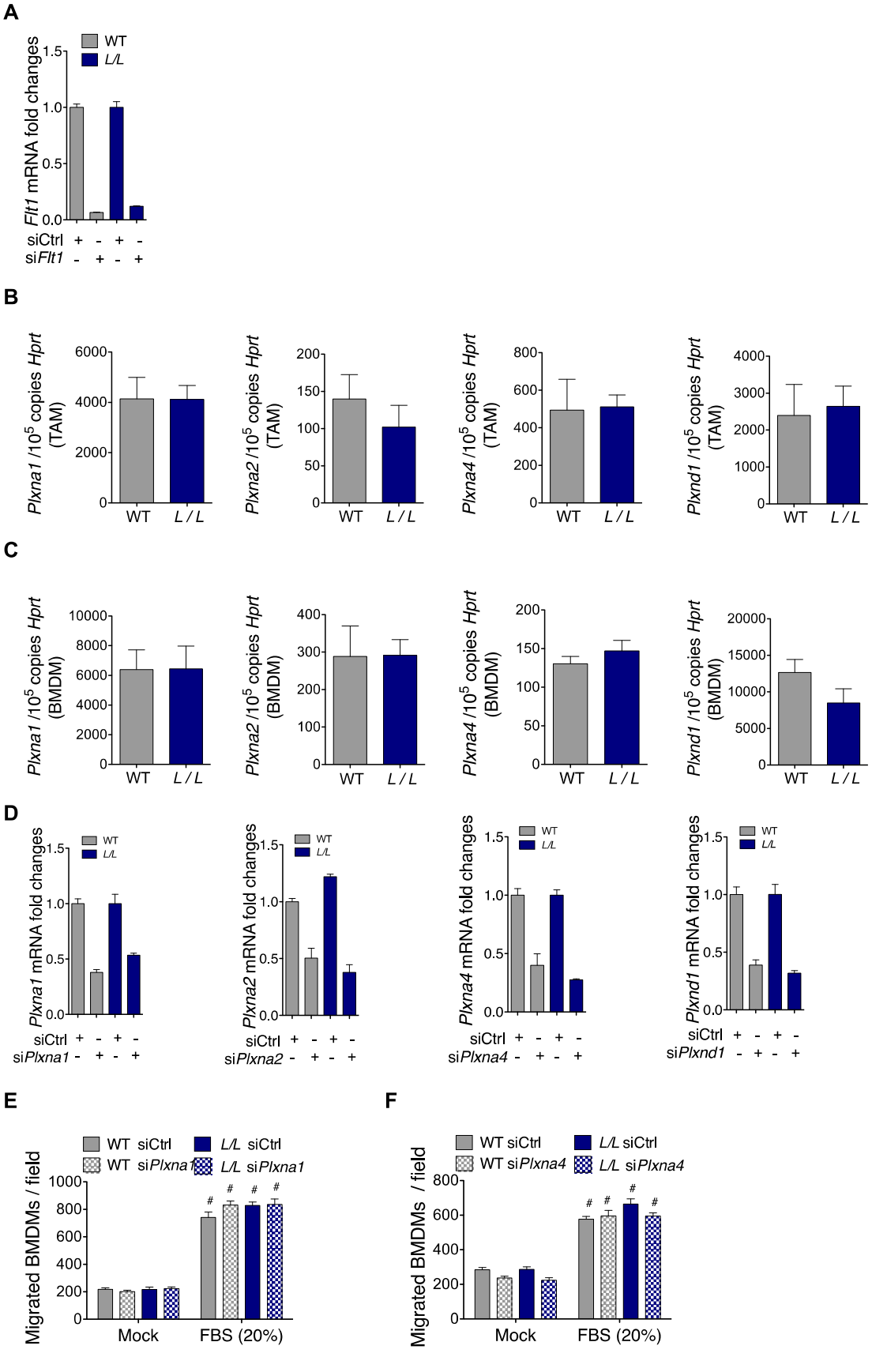
A
Flt1 mRNA fold changes
WT
L/L
siCtrl
siFlt1
B
Plxna1 /10^5 copies Hprt (TAM)
Plxna2 /10^5 copies Hprt (TAM)
Plxna4 /10^5 copies Hprt (TAM)
Plxnd1 /10^5 copies Hprt (TAM)
WT
L / L
C
Plxna1 /10^5 copies Hprt (BMDM)
Plxna2 /10^5 copies Hprt (BMDM)
Plxna4 /10^5 copies Hprt (BMDM)
Plxnd1 /10^5 copies Hprt (BMDM)
D
Plxna1 mRNA fold changes
Plxna2 mRNA fold changes
Plxna4 mRNA fold changes
Plxnd1 mRNA fold changes
siPlxna1
siPlxna2
siPlxna4
siPlxnd1
E
F
WT siCtrl
WT siPlxna1
L/L siCtrl
L/L siPlxna1
WT siPlxna4
L/L siPlxna4
Migrated BMDMs / field
Mock
FBS (20%)

FIGURE S5, RELATED TO FIGURE 7.

(A) Efficiency of *Flt1* silencing in WT and *Nrp1*-KO (*L/L*) BMDMs. **(B,C)** Transcript levels of *Plxna1*, *Plxna2*, *Plxna4*, and *Plxnd1* in TAMs (B) or BMDMs (C) isolated from WT and LysM-Cre;$Nrp1^{L/L}$ (*L/L*) mice. **(D)** Efficiency of *Plxna1*, *Plxna2*, *Plxna4* or *Plxnd1* silencing in WT and *Nrp1*-KO (*L/L*) BMDMs. **(E,F)** Migration of WT and *Nrp1*-KO (*L/L*) BMDMs, silenced for either *Plxna1* (E) or *Plxna4* (F), towards a gradient of fetal bovine serum (FBS). *$p<0.05$ versus WT; $^{\#}p<0.05$ versus mock. All graphs show mean ± SEM of 3 independent experiments.

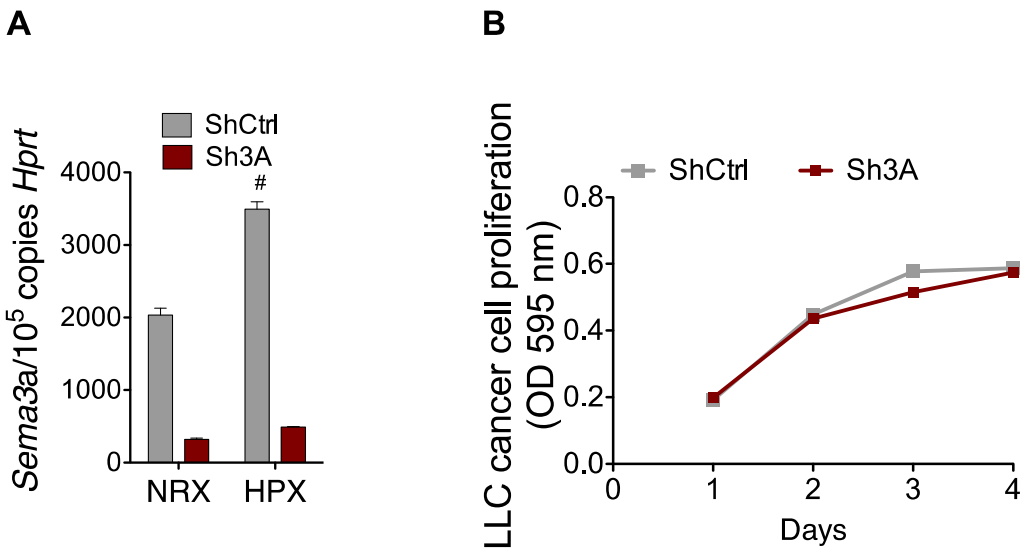

FIGURE S6, RELATED TO FIGURE 8.

(A) RNA levels of *Sema3a* in normoxic (NRX; 21% O_2) and hypoxic (1% O_2; HPX) LLC ShCtrl or LLC Sh3A cancer cells, transduced respectively with a lentiviral vector carrying a scramble sequence or a short-harpin RNA against *Sema3a*. n=3. **(B)** Cell growth curve of LLC-ShCtrl or LLC-Sh3A cancer cells in vitro, obtained by staining with crystal violet and absorbance quantification at 595 nm. n=3. $^{\#}p<0.05$ versus normoxia (NRX). All graphs show mean ± SEM.

SUPPLEMENTAL EXPERIMENTAL PROCEDURES

Animals: C57BL/6 *Hif1a* or *Hif2a* floxed mice were obtained from our mouse facility, and intercrossed with LysM-Cre mice. C57BL/6 *Ikbkb* floxed mice were obtained from M. Karin (UCSD, San Diego, CA), and intercrossed with LysM-Cre mice. C57BL/6 LysM-Cre and FVB MMTV-PyMT mice were purchased from Charles River. FVB MMTV-PyMT mice were then backcrossed in a C57BL/6 background in our facility. iCSF1R-Cre were kindly provided by J. Pollard (Albert Einstein College of Medicine, New York, NY). Acute deletion of *Nrp1* was obtained by i.p. injection of tamoxifen (1mg/mouse/day) for 5 days before subcutaneous implantation of LLC cancer cells in WT and iCSF1R-Cre;$Nrp1^{L/L}$ mice. C57BL/6 $Nrp1^{L/L}$ and $Nrp1^{Sema-}$ mice were kindly provided by C. Gu (Harvard University, Cambridge, MA) and D.D. Ginty (Johns Hopkins, Baltimore, MD). $Nrp1^{Sema-}$ mice were in 75% C57BL/6, thus postponing early post-natal lethality in the latter (Joza et al., 2012). In all the experiments, littermate controls were used. Housing and all experimental animal procedures were approved by the Institutional Animal Care and Research Advisory Committee of the K.U. Leuven.

Tumor models: Lewis lung carcinoma (LLC) adherent growing murine cells were harvested and single-cell suspensions of 2×10^6 in 200 µl of PBS were injected subcutaneously into the right flank of syngeneic mice. Tumor volumes were measured three times a week with a caliper and calculated using the formula: $V = \pi \times [d^2 \times D] / 6$, where d is the minor tumor axis and D is the major tumor axis. At

the sacrifice, tumors were weighed and collected for histological examination. Lung metastatic nodules were contrasted after intratracheal injection of 15% India ink solution. Superficial metastatic nodules were assessed under a stereomicroscope. Intrathoracic injections were performed following previous protocol with minor modifications (Cui et al., 2006). Briefly, 1×10^6 LLC cancer cells were harvested and resuspended in 35 µl PBS and diluted with an equal volume of growth factor-reduced Matrigel. Matrigel rapidly generates a gel formation at room temperature or above and acts as an anchor to prevent tumor cells from diffusing and spreading in the thorax after intrathoracic injection. Cell suspensions and injection kit were kept on ice until injection. Mice were anesthetized and were placed in the left lateral decubitus position. One-ml tuberculin syringes with 30-gauge hypodermic needles were used to inject the cell inoculum percutaneously into the right lateral thorax, at the lateral dorsal axillary line, approximately 1.5 cm above the lower rib line just below the inferior border of the scapula. The needle was quickly advanced approximately 6 mm into the thorax and quickly removed after the injection. Afterwards, the mouse was turned to the right lateral decubitus position. Animals were observed for 30 min until fully recovered. At day 16 mice were sacrificed and lung tumor removed and weighted. Parental Panc02 cells were orthotopically implanted into the pancreas as previously described (Mazzone et al., 2009). Briefly, mice were anesthetized with isoflurane, the stomach exteriorized via abdominal midline incision, and 1×10^6 Panc02 tumor cells in 30 µl PBS were injected into the head of the pancreas using a 29-gauge needle. Peritoneum and abdominal wall were

closed with individual surgical sutures. At day 14, primary tumors were removed and weighted, mesenteric lymph node metastases were recorded.

TPA model of acute skin inflammation: The phorbol ester TPA was used to induce acute skin inflammation as described before (Cramer et al., 2003). Briefly, TPA (2.5 μg in 20 μl acetone per mouse) was topically applied to the left outside ear of anaesthetized mice. The right ear was painted with acetone alone as a carrier control. Mice were sacrificed after 24 hr and the ear collected in 2% PFA for histological analysis.

BM transplantation and hematological analysis: C56BL/6 recipient mice were irradiated with 9.5 Gy. Subsequently, 1 x 10^7 BM cells from *Nrp1*$^{Sema-}$ mice were injected intravenously in the tail vein. Tumor experiments were initiated 6 weeks after BM reconstitution. Red and white blood cell count was determined using a hemocytometer on peripheral blood collected in heparin with capillary pipettes by retro-orbital bleeding.

Histology and immunostainings: For serial sections 7-µm-thick, tissue samples were immediately frozen in OCT compound or fixed in 2% PFA overnight at 4°C, dehydrated and embedded in paraffin. Forty-micrometer thick-sections were cut from snap-frozen tumor samples in OCT compound. Paraffin slides were first rehydrated to further proceed with antigen retrieval in citrate solution (DAKO). Cryo-sections were thawed in water and fixed in 100% methanol. If necessary, 0.3% H_2O_2 was added to methanol to block endogenous peroxidases. The sections were blocked with the appropriate serum (DAKO) and

incubated overnight with the following antibodies: rabbit anti-Neuropilin1 (Epitomics) 1:100, rat anti-CD31 (BD Pharmingen) 1:200, rabbit anti-FITC (Serotec) 1:200, goat anti-phosphohistone H3 (pHH3) (Cell Signaling) 1:100, rat anti-CD11b (BD Pharmingen) 1:100, rat anti-F4/80 (Serotec) 1:100, goat anti-MRC1 (R&D systems) 1:80, Alexa568-conjugated phalloidin (Life technologies) 1:200, rat anti-CD8 (BioXCell clone 53-6.72). Appropriate secondary antibodies were used: Alexa488 or Alexa546-conjugated secondary antibodies (Molecular Probes) 1:200, HRP-labeled antibodies (DAKO) 1:100. When necessary, Tyramide Signaling Amplification (Perkin Elmer, Life Sciences) was performed according to the manufacturer's instructions. Whenever sections were stained in fluorescence, ProLong Gold mounting medium with DAPI (Invitrogen) was used. Otherwise, 3,3'-diaminobenzidine was used as detection method followed by Harris' haematoxilin counterstaining, dehydration and mounting with DPX. Apoptotic cells were detected by the TUNEL method, using the AptoTag peroxidase in situ apoptosis detection kit (Millipore) according to the manufacturer's instructions. Microscopic analysis was done with an Olympus BX41 microscope and CellSense imaging software or a Zeiss Axioplan microscope with KS300 image analysis software.

Hypoxia assessment and tumor perfusion: Tumor hypoxia was detected 1 hr after i.p. injection of 60 mg/kg pimonidazole hydrochloride into tumor-bearing mice. Mice were sacrificed and tumors harvested. To detect the formation of pimonidazole adducts, tumor cryosections were immunostained with Hypoxyprobe-1-Mab1 (Hypoxyprobe kit, Chemicon) following the manufacturer's

instructions. To quantify in vivo *Sema3a* and *Vegfa* RNA levels in hypoxic versus normoxic fractions of the tumor, LLC subcutaneous tumors were minced in RPMI medium containing 0.1% collagenase type I and 0.2% dispase type I (30 min at 37°C), passed through a 19 G needle and filtered. After RBC lysis, cells were fixed using citofix/citoperm (BD Pharmingen) in presence of 12.5 units of RNAseOUT^{TM} (Life technologies) for 20 min at 4°C. After washing, the single cell suspensions were stained with Hypoxyprobe-1-Mab1 (Hypoxyprobe kit, Chemicon) for 30 min at 37°C and sorted using a BD FACSAria II (BD Biosciences). PIMO-positive and PIMO-negative sorted cells were finally collected in RLT buffer (Quiagen) and RNA was isolated following the manufacturer's instructions. The same procedure was applied to isolate hypoxic (PIMO-positive) and normoxic (PIMO-negative) TAMs, gated for the macrophage marker F4/80, as it was previously described (Movahedi et al., 2010). Perfused tumor vessels were counted on tumor cryosections from mice injected intravenously with 0.05 mg FITC-conjugated lectin (Lycopersicon esculentum; Vector Laboratories).

Bone marrow derived macrophages (BMDMs): Macrophages were derived from BM precursors as described before (Meerpohl et al., 1976). Briefly, BMDMs (1.6 x10^6 cells/ml) were cultured in a volume of 6 ml in a 10 cm Petri dish (non tissue culture treated, bacterial grade) in DMEM supplemented with 20% FBS and 30% L929 conditioned medium as a source of M-CSF. After 3 days of culture, an additional 3 ml of differentiation medium was added. At day 7, macrophages were detached with ice cold PBS and characterized by FACS,

using the pan-macrophage marker F4/80. For the *in vitro* M1 or M2 polarization, BMDMs were stimulated for additional 72 hours with 20 ng/ml IFNγ + 100 ng/ml LPS or 10 ng/ml IL4 respectively.

FACS analysis and flow sorting of tumor-associated cells: LLC tumor-bearing mice were sacrificed by cervical dislocation and tumors were harvested. Tumors were minced in RPMI medium containing 0.1% collagenase type I and 0.2% dispase type I and incubated in the same solution for 30 min at 37°C. The digested tissue was passed 10 times through a 19G needle, filtered using a 70 µm pore sized mesh and centrifuged 5 min at 1000 rpm. Red blood cell lysis was performed using Hybri-Max™ (Sigma-Aldrich). Cells were resuspended in FACS buffer (PBS containing 2% FBS and 2 mM EDTA) and incubated for 15 min with Mouse BD Fc Block™ purified anti-mouse CD16/CD32 mAb (BD-pharmingen) and stained with the following antibodies for 20 min at 4 °C: anti-F4/80 antibody (BM8, eBioscience), anti-CD115 (AFS98, eBioscience), anti-CD3 (17A2), anti-CD4 (RM4-5), anti-CD8a (53-6.7), Ly6C (AL-21), anti-Ly6G (1A8), anti-CD11b (M1/70) (all from BD Biosciences). FACS analysis on BMDM proliferation and apoptosis were performed using FITC BrdU Flow Kit (BD Bioscience) and FITC Annexin V (BD Bioscience) respectively according with manufacturer's instructions. Cells were subsequently washed and resuspended in cold FACS buffer before FACS analysis or flow sorting by a FACS Canto II or FACS Aria (BD Biosciences), respectively.

BMDM electroporation: Silencing of *Flt1*, *Plxna1*, *Plxna*2, *Plxna*4, or *Plxnd1* was achieved by electroporation with specific siRNAs. Overexpression of p50

and p65 was achieved by electroporation with specific plasmids purchased from Addgene (Plasmid 20018: p50 cFlag pcDNA3 and Plasmid 20012: RelA cFlag pcDNA3). Briefly, 2.4 x 10^6 BMDMs were resuspended in 320 µl of Opti-MEM and were electroporated (250V, 950 mF, ∞ Ω) with 10 µg of each of two plasmids (p50 and p65) or with 120 pmol of one siRNA alone, or 60 pmol of each of two siRNAs in combination. Commercially available siRNAs were purchased from Invitrogen and their sequences or assay IDs are listed below:

siRNA	**ID**
Plxna1	MSS207786 and MSS276393, alone or in combination
Plxna2	MSS207788 and MSS276394, alone or in combination
Plxna4	MSS216812 and MSS216813, alone or in combination
Plxnd1	MSS228671 and MSS228673, alone or in combination
Flt1	66936 and 67029, alone or in combination
Scrambled Ctrl	Negative control medium GC: 12935-300

Nitric oxide (NO) measurement: For NO, nitrite (NO_2^-) quantification was assayed by a standard Greiss reaction. 3×10^5 sorted TAMs or activated BMDMs (20 ng/ml IFNγ + 100 ng/ml LPS for 24 hr) were plated in 200 µl RPMI (supplemented with 10% FBS) in flat-bottom 96 well plates. Culture supernatant (100 µl) was mixed with 100 µl of 1% sulfanilamide, 0.1% N-(1-naphthyl)ethylenediamine dihydrochloride, and 2.5% H_3PO_4 (Greiss reagent,

Sigma-Aldrich). Absorbance was measured at 540 nm in a microplate reader and normalized with a sodium nitrite standard curve.

Cell migration assay: In vitro migration of macrophages and endothelial cells (ECs) was assessed by using a 8 μm-pore transwell system (Corning Life Science). To determine macrophage migration in normoxia and hypoxia (1% O_2), 5 x 10^5 BMDMs were resuspended in DMEM supplemented with 2% FBS and seeded in the upper chamber of a polyethylene terephthalate (PET) membrane transwell, while the lower chamber contained DMEM supplemented with 2% FBS and 100 ng/ml Sema3A, 50 ng/ml $VEGF_{120}$, 50 ng/ml $VEGF_{164}$, 50ng/ml SDF1 or 50ng/ml CCL21 (R&D). For macrophage migration in hypoxia, all manipulations were executed in a hypoxic glove box incubator (Coy Laboratory Products). To determine the ability of macrophage to promote EC migration, 2.5×10^5 BMDMs or sorted TAMs were seeded in the lower chamber in M199 medium supplemented with 2% FBS. After 36 hr preconditioning, 10^4 HUVECs were seeded in M199 2% FBS in the upper chamber of a polycarbonate membrane transwell. After 8 hr, migrated cells were fixed with 4% PFA, stained with crystal violet and counted under the microscope.

In vivo migration assay: To assess the chemoattraction of Sema3A and VEGF isoforms in vivo, 6-week-old mice were subcutaneously injected with 500 μl of growth factor–reduced Matrigel (BD Biosciences), supplemented with either PBS or with 1 μg purified murine Sema3A, $VEGF_{164}$ or $VEGF_{120}$ (R&D). After 5 days, the mice were sacrificed and matrigel plugs fixed in 2% paraformaldehyde.

Macrophage recruitment was evaluated by histological detection with a rat anti-mouse F4/80 antibody (Serotec).

Cytoskeleton elongation ratio: The motility of macrophages in response to specific chemokines was determined by evaluating the actin cytoskeleton elongation as described before (Wheeler et al., 2006). Briefly, BMDMs (2×10^4) were seeded onto 13-mm glass coverslips in DMEM 10% FBS growth medium. Cells were starved for 16 hr and then stimulated with 100 ng/ml Sema3A or 50 ng/ml $VEGF_{164}$ (R&D Systems). BMDMs were fixed in 2% PFA for 20 min for analysis of F-actin. Cells were permeabilised with 0.2% Triton X-100 and blocked with 20% goat serum in PBS. F-actin was visualized with TRITC-conjugated phalloidin (Sigma-Aldrich). Images of cells were acquired with a Olympus BX41 microscope, using a 40×/1.30 Plan Neofluar objective and the accompanying Cellsense Olympus software. Each image was then converted into a binary threshold image, and the longest chord (length), and the widest chord perpendicular to this chord (width) was measured. The elongation of the cell was calculated by dividing the length by the width.

EC capillary formation: The ability of macrophages to induce the formation of an EC capillary network was assessed by both co-culturing ECs and macrophages, and stimulating ECs with macrophage-derived conditioned medium. 10^5 BMDMs or sorted TAMs were embedded in 50 μl Matrigel (BD bioscience) diluted ½ in M199 medium supplemented with 5% FBS and seeded in flat bottom 96 well plates. After 1 hr solidification, 25 μl M199 medium

supplemented with 2.5% FBS was added. After 36 hr of medium preconditioning, 10^4 HUVECs, fluorescently labeled with PKH-26 (Sigma Alderich), were added to the Matrigel in 25 μl M199 supplemented with 2.5% FBS. Alternatively, 2.5 x 10^5 BMDMs or sorted TAMs were seeded in M199 supplemented 2.5% FBS in flat bottom 96 well plates. After 36 hr, cell-free conditioned medium was harvested and used to resuspend 1×10^4 HUVECs which were then seeded directly on 50 μl solidified Matrigel diluted ½ in M199 medium supplemented with 5% FBS in 96 well plates. After 4 hr, HUVEC capillary formation was stopped and fixed with 4% PFA. Pictures were taken with a inverted microscope and capillary formation was analyzed by measuring the number and length of branches using the "Angiogenesis Analyzer" plugin with ImageJ (http://image.bio.methods.free.fr/ImageJ/?Angiogenesis-Analyzer-for-ImageJ&lang=en).

Macrophage cytotoxicity assay: To evaluate the cytotoxic ability of macrophages against cancer cells, LLC cells were first labeled with 1μCi/ml ^{3}H-Thymidine in DMEM supplemented with 10% FBS for 20 hr. Next, 1×10^4 labeled LLC cells were seeded together with increasing concentrations of activated BMDMs (20 ng/ml IFNγ + 100 ng/ml LPS, 24h) or sorted TAMs (1/1 up to 1/16). After 24 hr, LLC cell death was detected by measuring radioactivity in cell-free medium as counts per min (cpm) on a Wallac 1450 Liquid Scintillation Counter. The histogram shown represents the cytotoxicity of 1.6×10^5 macrophages towards 1×10^4 LLC cells.

T-cell suppression: For T cell suppression assays, 2×10^5 naive C57/Bl6 splenocytes were added to increasing concentrations of BMDMs or sorted TAMs (1/4 up to 1/16), in flat-bottom 96-well plates. These cocultures were promptly stimulated with 1 µg/ml anti-CD3. After 24 hr, cells were pulsed with ^{3}H-thymidine (PerkinElmer) and incubated for another 18 hr before incorporated radioactivity was measured as counts per min (cpm) on a Wallac 1450 Liquid Scintillation Counter. The histogram shown represents the suppression of 2×10^5 activated T cells by 5×10^4 macrophages.

T-cell depletion: Th cells and CTLs were depleted in LLC tumor-bearing mice by i.p. injection of 0.2 mg anti-CD4 (GK1.5) or anti-CD8 (53-6.7) (BioXCell), respectively, every third day, starting the sixth day after tumor injection. Control mice were treated with the same doses of rat IgG isotypes.

Protein extraction and immunoblot: Protein extraction was performed using extraction buffer (20 mM Tris HCl, 150mM NaCl, 1% Triton X-100, 10% glycerol, 5 mM EDTA). The following antibodies were used: VEGFR1 (Sigma-Aldrich) and pVEGFR1 (Tyr1213, Millipore). Signal was detected using ECL system (Amersham Biosciences) according to the manufacturer's instructions.

QRT-PCR: Quantitative RT-PCR was performed as described (Fischer et al., 2007), using commercially available or homemade primers and probes for the studied genes. The assay IDs or the sequences of primers and probes (when home-made) are listed below:

Gene	**Assay ID (company)/primer sequences when home-made**
Hprt	Mm.PT.47.12014145 (Integrated DNA technologies)
Nrp1	Mm.PT.47.7307239 (Integrated DNA technologies)
Vegfa	Mm00437304_m1 (Applied Biosystems)
Sema3a	FW: CCTCGCTCGGGACCCTT RV: CTTTGCAGTAGGAAAATAGCGTGA Probe: CATGAGGACCCATCCCATGCACAG
Plxna1	FW: GGTGGGACCCTCCTAACAGTC RV: TTTCCCTCTCAATGCCTCCAT Probe: TGAACCTCGAATCCGCGCCAA
Plxna2	FW: AATGTATGCACAGTGGTAAACACAA RV: GTCGTTATAGATGAGTAAGGATTGAACA Probe: ATCCAAACTCATCTGGCCGTTCCACA
Plxna3	FW: GCAATCGTGTGTATCTCACCTGTC RV: ACCGTAGGGTCCTGGGTGTAG Probe: AGCCCTATCACCCTTGCCATCGATCAT
Plxna4	Mm00558881_m1 (Applied Biosystems)
Plxnd1	Mm.PT.47.7144309 (Integrated DNA technologies)
Nos2	Mm.PT.47.5457635 (Integrated DNA technologies)
Cxcl9	Mm.PT.47.16060565 (Integrated DNA technologies)
Cxcl10	Mm00445235_m1 (Applied Biosystems)
Cxcl11	Mm00444662_m1 (Applied Biosystems)
Il2	Mm99999222_m1 (Applied Biosystems)

Il12	Mm00434169_m1 (Applied Biosystems)
Il10	Mm00439614_m1 (Applied Biosystems)
Arg1	Mm.PT.47.13791410 (Integrated DNA technologies)
Ym1	Mm00657889_mH (Applied Biosystems)
Ccl21	Mm03646971_gH (Applied Biosystems)
Ccl22	Mm00436439_m1 (Applied Biosystems)
Ifng	Mm00801778_m1 (Applied Biosystems)
Il6	Mm01210733_m1 (Applied Biosystems)
Il4	Mm.PT.51.5378743 (Integrated DNA technologies)
Ikbkb	Mm.PT.56a.8834084 (Integrated DNA technologies)
Ikbkg	Mm.PT.56a.11436481 (Integrated DNA technologies)

Sema3A cell-binding assays: Expression constructs encoding m-Sema3A, m-Sema3A fused with secreted placental Alkaline Phosphatase (Sema3A-AP), and m-Sema3E-AP fusion were transfected in COS cells by DEAE-Dextran method. Recombinant proteins released in conditioned media were semi-purified by size fractionation, using protein concentrator devices (Centricon, Millipore). In situ binding assays were performed with a modification of the protocol described previously (Tamagnone et al., 1999). In particular, 2×10^5 BMDMs were grown for 16 hr in a 48-multiwell culture dish, and then incubated for 1 hr at 4°C with complete medium containing 8 nM of recombinant semaphorins in presence of 50 μg/ml Heparin. After 5 washes, cells were fixed, heated for 10 min at 65°C to inactivate endogenous phosphatases, and incubated with NBT–BCIP (nitro blue

tetrazolium–5-bromo-4-chloro-3-indolyl-phosphate) AP substrate (Promega) for in situ cell staining. For a quantitative assessment of ligand binding in presence of unlabeled competitor, cell-bound AP was revealed by incubation with the chromogenic soluble AP-substrate p-nitrophenylphosphate (Sigma), then measured by a multiwell spectrophotometer (absorbance at 405 nm).

Statistics: The data were represented as mean ± SEM of the indicated number of measurements. Statistical significance was calculated, using Prism (GraphPad Inc.), by two-tailed unpaired t-test for two data sets, Chi-square for MMTV-PyMT tumor staging, and Gehan-Breslow-Wilcoxon for the survival upon orthotopic LLC tumor implantation, with $p<0.05$ considered statistically significant.

SUPPLEMENTAL REFERENCES

Cramer, T., Yamanishi, Y., Clausen, B.E., Forster, I., Pawlinski, R., Mackman, N., Haase, V.H., Jaenisch, R., Corr, M., Nizet, V.*, et al.* (2003). HIF-1alpha is essential for myeloid cell-mediated inflammation. Cell *112*, 645-657.

Cui Z.Y., Ahn J.S., Lee J.Y., Kim W.S., Lim H.Y., Jeon H.J., Suh S.W., Kim J.H., *et al.* (2006). Mouse Orthotopic Lung Cancer Model Induced by PC14PE6. Cancer Res Treat. *38,* 234-239

Fischer, C., Jonckx, B., Mazzone, M., Zacchigna, S., Loges, S., Pattarini, L., Chorianopoulos, E., Liesenborghs, L., Koch, M., De Mol, M.*, et al.* (2007). Anti-PlGF inhibits growth of VEGF(R)-inhibitor-resistant tumors without affecting healthy vessels. Cell *131*, 463-475.

Joza, S., Wang, J., Fox, E., Hillman, V., Ackerley, C., and Post, M. (2012). Loss of semaphorin-neuropilin-1 signaling causes dysmorphic vascularization reminiscent of alveolar capillary dysplasia. Am J Pathol *181*, 2003-2017.

Meerpohl, H.G., Lohmann-Matthes, M.L., and Fischer, H. (1976). Studies on the activation of mouse bone marrow-derived macrophages by the macrophage cytotoxicity factor (MCF). Eur J Immunol *6*, 213-217.

Tamagnone L., Artigiani S., Chen H., He Z., Ming G.I., Song H., Chedotal A., Winberg M.L., Goodman C.S., Poo M., *et al.* (1999). Plexins are a large family of receptors for transmembrane, secreted, and GPI-anchored semaphorins in vertebrates. *Cell* 99, 71-80.

Wheeler, A.P., Wells, C.M., Smith, S.D., Vega, F.M., Henderson, R.B., Tybulewicz, V.L., and Ridley, A.J. (2006). Rac1 and Rac2 regulate macrophage morphology but are not essential for migration. J Cell Sci *119*, 2749-2757.